Detecting and gettering chromium impurities in photovoltaic crystalline silicon

ARCHIVES
MASSACHUSETTS INSTITUTE OF TECHNOLOGY
JUL 30 2015
LIBRARIES

by

Mallory Ann Jensen

B.S. in Mechanical Engineering
University of Pennsylvania, 2010

Submitted to the Department of Mechanical Engineering
in partial fulfillment of the requirements for the degree of
Master of Science in Mechanical Engineering

at the

MASSACHUSETTS INSTITUTE OF TECHNOLOGY

June 2015

© 2015 Massachusetts Institute of Technology. All rights reserved.

Author..... Signature redacted
Department of Mechanical Engineering
May 8, 2015

Certified by..... Signature redacted
Tonio Buonassisi
Associate Professor of Mechanical Engineering
Thesis Supervisor

Accepted by..... Signature redacted
David E. Hardt
Professor of Mechanical Engineering
Chairman, Department Committee on Graduate Theses

Detecting and gettering chromium impurities in photovoltaic crystalline silicon

by

Mallory Ann Jensen

Submitted to the Department of Mechanical Engineering
on May 8, 2015 in Partial Fulfillment of the
Requirements for the Degree of Master of Science in
Mechanical Engineering

ABSTRACT

Photovoltaic (PV) modules provide a source of renewable electricity by harnessing solar energy. Currently, crystalline silicon dominates the PV market with an approximate market share of 90% and record solar cell efficiencies greater than 20%. However, the PV market must decrease the cost to the consumer to maintain growth and meet global electricity demands. Increasing the solar-to-electricity conversion efficiency is one of the most significant cost levers.

Transition metal impurities can degrade silicon wafer-based solar cell efficiencies at concentrations as low as 10^{10} cm^{-3}. By removing interstitial metals from the bulk and/or collecting interstitial metals at heterogeneous nucleation sites, phosphorous diffusion gettering renders them less detrimental in the final solar cell. While they exist for iron, kinetics process simulation tools do not yet exist for chromium, which has higher capture cross-sections for minority carriers and is therefore more detrimental in both *p*- and *n*-type materials.

In this thesis, I employ synchrotron-based X-ray fluorescence microscopy to study chromium (Cr) distributions in multicrystalline silicon in as-grown material and after two phosphorous diffusion profiles. I complement quantified precipitate size and spatial distribution with interstitial Cr concentration and minority carrier lifetime measurements to provide insight into chromium gettering kinetics and offer suggestions for minimizing the device impacts of chromium. The data presented in this thesis can be used in development of kinetics process simulation tools for chromium gettering.

Finally, I describe a new technique for detecting low concentrations of impurities in *n*- and *p*-type silicon. The development of high-performance silicon materials, including *n*-type, necessitates more sensitive impurity detection techniques, capable of measuring interstitial contaminations below 10^{10} cm^{-3}. I propose the development of a free-carrier absorption-based technique that incorporates a temperature stage. By measuring injection-dependent lifetimes at a wide range of sample temperatures, the identifying parameters of lifetime-limiting defects can be deduced.

Thesis Supervisor: Tonio Buonassisi
Title: Associate Professor of Mechanical Engineering

ACKNOWLEDGEMENTS

After graduating from UPenn and joining Nestlé, I never imagined that I would be at MIT studying solar cells and aspiring to a career in the PV industry. It has been an incredible journey so far and I am so grateful to have been given this opportunity. I would like to thank my parents and my sisters for not questioning my decision to enroll in graduate school and move to Boston, and for being fully supportive and loving during the transition. I would not be where I am now without you. I would also like to thank Joe, who has dealt with my stress and anxiety and offered unfailing support and encouragement.

I would like to thank Prof. Buonassisi for taking a chance on a student with no previous experience, and encouraging me throughout the learning process. Your enthusiasm for solar is contagious, and I hope to one day be as knowledgeable in the field as you are.

I would like to acknowledge the very supportive current and former members of the MIT PV Lab for inspiring me to learn and become passionate about photovoltaics. I would especially like to thank those who have supported and encouraged me while completing my thesis work: Dr. Jasmin Hofstetter for guidance and expertise throughout the entire project; Ashley Morishige for experimental support, guidance, and close reading of my thesis; Dr. David Fenning for sourcing the intentionally-contaminated samples and provided mentorship and teaching especially during beamline measurements and manuscript preparation; Dr. Doug Powell for giving freely of his time and efforts to mentor me when I first joined the lab; Dr. Sin Cheng Siah for teaching me about free-carrier absorption and informing my characterization tool design; and Dr. Marius Peters for close reading of my thesis. Thank you also to Dr. Gianluca Coletti for growing the chromium-contaminated ingots for this study and for providing input on the data analysis and conclusions and to Dr. Barry Lai at Argonne National Laboratory for assistance in processing the μ-XRF data.

This research was made possible by funding from the National Science Foundation Graduate Research Fellowship Program and grants from the National Science Foundation and the U.S. Department of Energy.

CONTENTS

FIGURES

TABLES

CHAPTER

1

INTRODUCTION

1.1 Motivation: Cost, efficiency, and lifetime

Decreasing the cost of photovoltaic (PV) modules is a significant and urgent challenge. The PV industry has grown rapidly over the last 15 years: installed, grid-connected PV capacity grew from 1.3 GW_p in 2000 to 139 GW_p in 2014 [1]. Despite this rapid growth, solar PV accounted for less than 1% of the global electricity production in 2013. To reach 4,500 TWh per year installed PV capacity (11% global electricity production), projected by the International Energy Agency by 2050, current manufacturing capacity must be scaled quickly and cost-effectively [2]. Since area-dependent costs (*e.g.,* module materials and installation hardware) scale inversely with module efficiency, one of the most effective ways to reduce the installed system cost is to increase this solar-to-electricity conversion efficiency [3], [4]. This is shown in Figure 1, reproduced from [5], where efficiency is located in the top right of the sensitivity plot.

Over 90% of the solar cells manufactured today comprise crystalline silicon. Single-crystalline silicon (sc-Si) held a market share of approximately 35% in 2014, while multicrystalline silicon (mc-Si) held a market share of approximately 55% [6]. Due to a simpler manufacturing process in which polysilicon is melted and re-solidified in a crucible, the area cost ($\$/m^2$) of mc-Si wafers is lower than that of sc-Si wafers which are typically made by the Czochralski crystal-pulling method. In 2013, the estimated manufacturing cost of a standard mc-Si module was US$0.92/$W_p$, with a minimum sustainable price of US$1.11/$W_p$ [5]. The minimum sustainable price tracks with the manufacturing cost and is a metric used to separate the market price from the finances of the manufacturer.

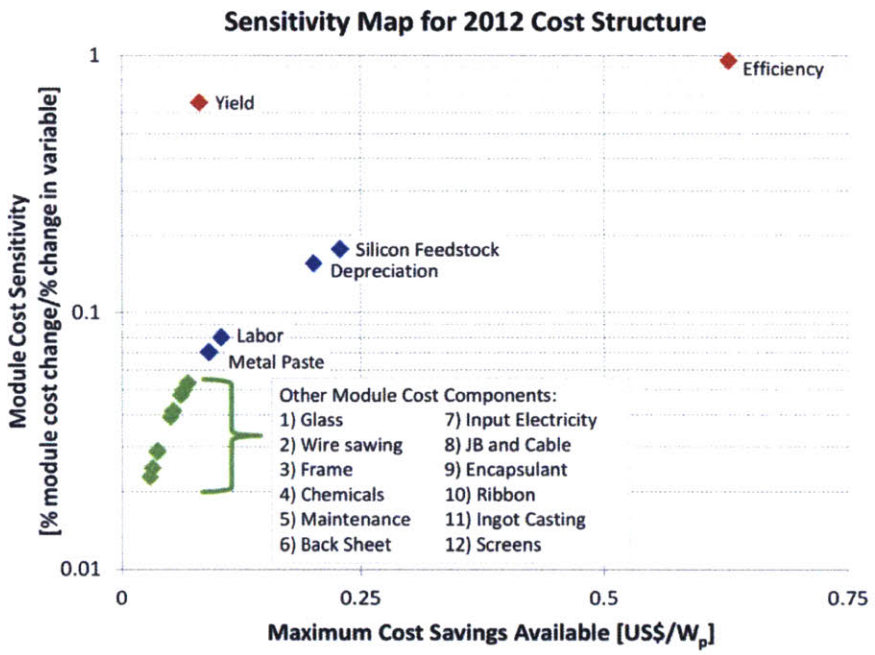

Figure 1: Photovoltaic module cost sensitivity

This figure is reproduced from [5]. The module cost sensitivity is plotted versus the available cost savings to elucidate the most important parameters to reduce module-manufacturing cost. Efficiency, located in the top right corner, is one of the most important levers to reduce the cost per peak watt.

A key innovation area in crystalline silicon is continued optimization of lower-cost materials, including mc-Si. The record research-scale solar cell efficiency for mc-Si is 20.8% in 2015, held by Trina Solar, and the record efficiency for a sc-Si solar cell in 2015 is 25.6%, held by Panasonic with the Heterojunction with Intrinsic Thin layer (HIT) solar cell architecture [7]. Efficiencies of mc-Si solar cells are typically lower than sc-Si cells due to an abundance of metal impurities such as iron [8], [9]. In addition, the distribution of mc-Si solar cell efficiencies from an ingot normally include a low efficiency "tail," which has in part been attributed to grain boundaries and the multiplication of dislocations during growth [10].

A typical mc-Si solar cell configuration is shown in Figure 2 below. Incident light with energy above the bandgap of silicon (1.124 eV [11]) is absorbed to produce free carriers – one electron in the conduction band and one hole in the valence band for each photon. A *pn*-junction separates these carriers into electrons and holes for extraction as usable current in the external circuit, which can be electricity for a home, a business, or the grid. The solar cell conversion efficiency is defined as the ratio of output power (the number of carriers that reach the external

circuit) to incident power (the number of photons approaching the module before any protective layers such as glass). In a simple approximation for silicon solar cells, free carriers near the junction are transported across by drift due to the electric field at the junction. Far away from the junction, diffusion due to concentration gradients determines free carrier motion. For separation to occur, free carriers must be allowed sufficient time after excitation to diffuse to the junction and then from the junction to either the front or back contact of the solar cell.

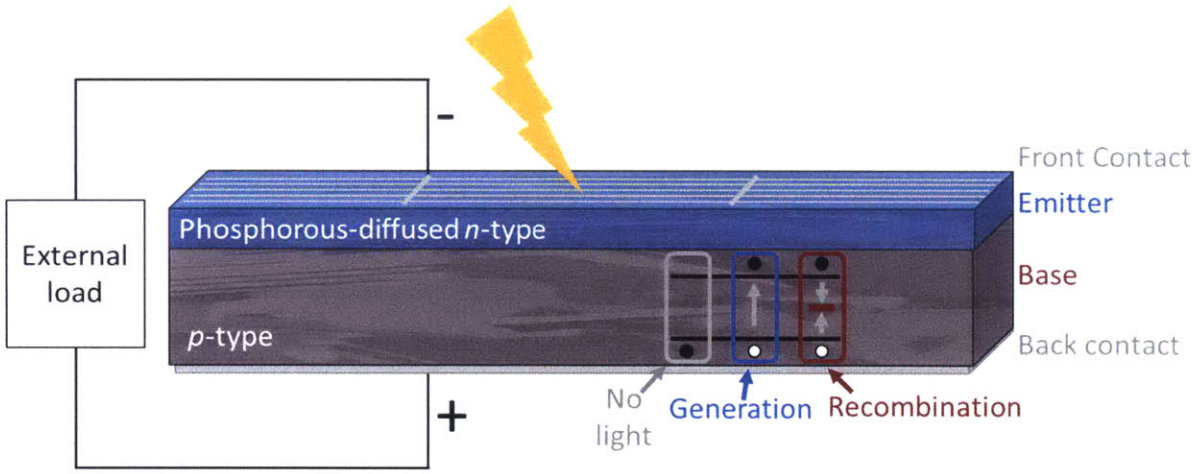

Figure 2: Diffused-junction multicrystalline silicon solar cell configuration

Schematic of a standard *p*-type mc-Si solar cell, with an *n*-type emitter produced by phosphorous diffusion. When light is absorbed by the solar cell, free carriers (electrons and holes) are produced. The *pn*-junction located between the emitter and base separates electrons and holes for extraction through the back or front contacts as usable current. Figure adapted from [11].

Carrier separation and collection is often limited by non-ideal processes, during which carriers produce a photon that can be reabsorbed or recombine rather than reaching the external circuit. Recombination can take many different forms, as will be discussed in Chapter 2. In the presence of defects, depicted in the inset of Figure 2, recombination occurs after carriers are excited through an energy level located between the two bands. The amount of time that a carrier remains in an excited state before recombination is termed the "lifetime." In a *p*-type base, the dopant introduces a large number of holes into the material. As a result, holes are termed the "majority" carriers in this region, and electrons are termed "minority" carriers. Because majority carriers are abundant, the behavior of minority carriers limits the base lifetime. Minimizing recombination and therefore maximizing lifetime in the base material is essential for high

efficiency. PC1D [12] was used to model a simple solar cell like that shown in Figure 2 with parameters similar to those specified in Table I of [13]. The cell thickness was 180 μm. To assess the impact of lifetime on efficiency, the lifetime was varied between 0 and 300 μs and the efficiency at maximum base power was extracted. The results are plotted in Figure 3. At very low lifetimes (< 25 μs), efficiency increases linearly with lifetime. As lifetime increases past 100 μs, the efficiency begins to level off but still increases slowly with lifetime. This curve will be different for every solar cell configuration. For a solar cell with very low surface recombination velocities, low shunt resistances, and low contact resistances, small changes in base lifetime will have a more dramatic effect on efficiency.

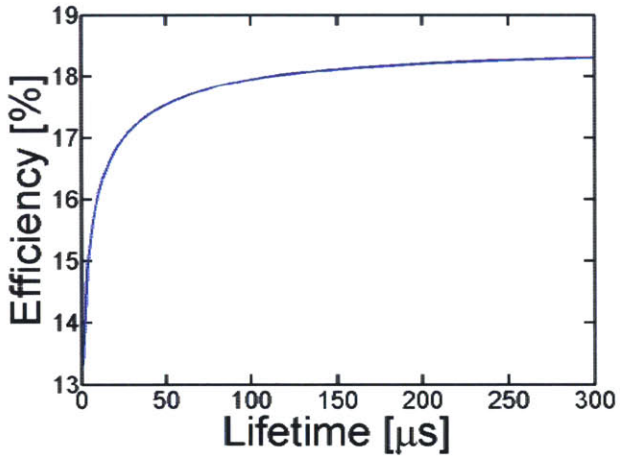

Figure 3: Efficiency as a function of lifetime

Solar cell efficiency is plotted as a function of base lifetime. Simulations were performed using a diffused junction configuration in PC1D with one internal shunt element, front surface reflectance, internal reflectance, and other parameters specified in [13].

The lifetime can also be expressed as a diffusion length using the following relation:

$$L_{\mathrm{D}} = \sqrt{D\tau} \tag{1}$$

where D is the diffusivity of the carrier at the solar cell operating temperature and τ is the carrier lifetime. The diffusion length is an important metric for intuitive understanding of solar cell operation: if the distance between the excited free carrier and the junction is much greater than the diffusion length, the probability for carrier collection will be low. If the carrier diffusivity is known, which is not always the case in novel materials, the diffusion length can be easily

calculated from a lifetime measurement. In this thesis, I will focus on the lifetime rather than the diffusion length, but it is important to remember that the two terms are closely related.

Metal impurities such as chromium and iron act as minority-carrier recombination centers through mid-gap energy states, limiting charge-carrier lifetimes at device-relevant excess-carrier densities [14], [15]. These metal impurities can be present as either single atoms within the lattice (interstitial or substitutional and especially detrimental) or precipitates. The impact of different metal impurities on solar cell efficiency has been studied through experiment and simulation with the conclusion that low concentrations of impurities can significantly degrade efficiency [16]–[18]. To prevent solar cell performance degradation by impurities, two approaches exist: 1) root-cause elimination and 2) management through gettering. In the first approach, the contaminant and its source must be identified. Chromium, for example, is a major component of stainless steel, which is often used in wafer-fabrication equipment. If stainless steel components are removed from the process, the amount of chromium contamination should decrease or become undetectable. Engineering impurity distributions through high-temperature gettering processes is an alternative approach when the root cause cannot be completely eliminated or when root-cause elimination is prohibitively expensive. There is some background contamination in the crucible material used to grow mc-Si ingots that cannot be removed – high-temperature gettering during phosphorous diffusion can reduce the impact of contaminants in this case.

Knowledge of the thermodynamics and kinetics of a contaminant can inform diffusion gettering profile design to mitigate the impurity impact on solar cell efficiency. Iron, for example, has been well-studied, and kinetics process simulation tools exist to engineer its distribution in the material [19]–[23]. In contrast, the impact of processing steps on chromium (both precipitated and interstitial) has not been studied as extensively, although the detrimental nature of the impurity is well-known. Interstitial chromium (Cr_i) is highly effective at capturing minority carriers: the capture cross-sections for chromium are 1.5 and 57 times larger than iron in *p*- and *n*-type silicon, respectively [18]. Chromium has been found to impact cell performance at concentrations as low as 10^{10} cm^{-3}, and the maximum allowable chromium contamination in the silicon melt ranges from 1×10^{15} cm^{-3} to 2×10^{17} cm^{-3} depending on the crystal growth method, device architecture, and target efficiency [17], [24], [25]. In this thesis, I will explore the gettering response of chromium impurities in mc-Si.

1.2 Prior work on Cr impurities in Si

As lifetimes of industrial materials have improved, interest in studying transition metal contamination in silicon has increased. Though not as omnipresent as iron, chromium has appeared in moderate concentrations in industrial samples [9]. Conzelmann *et al.* [26] presented one of the first studies regarding recombination due to chromium impurities in silicon. A defect level at 0.23 eV below the conduction band was attributed to interstitial chromium, while a distinctly different level at 0.27 eV above the valence band was attributed to chromium-boron pairs in *p*-type silicon [26]. Later, the defect parameters of chromium were refined through measurements by a variety of different techniques, including surface photovoltage, deep-level transient spectroscopy, and temperature- and injection-dependent lifetime spectroscopy [27]–[31]. Habenicht *et al.* [30] produced spatially resolved images of chromium point defect concentration in mc-Si samples by controlling the defect state and adapting the methods for iron point-defect measurements first proposed by [32].

At sufficiently high contamination levels and for a range of doping concentrations, chromium ions are favored to form precipitates. Bendik *et al.* [33] used electron paramagnetic resonance measurements to study the precipitation kinetics of intentionally chromium-contaminated silicon. Formation of chromium disilicide ($CrSi_2$) precipitates during crystallization has been confirmed by energy dispersive X-ray spectroscopy [34]. In mc-Si, precipitation at dislocations during cool-down after crystallization was predicted by numerical simulation [35] and implied by micro-photoluminescence techniques [36]. Schön *et al.* found that minority carrier lifetime increased and $[Cr_i]$ decreased after phosphorous diffusion gettering [35]. Other quantitative studies of the effect of phosphorous diffusion gettering have measured high chromium concentrations at near-surface regions, suggesting external gettering [37]–[39], as well as a reduction of the total bulk chromium concentration [40].

1.3 Approach

In this thesis, I hypothesize that the distribution of chromium in silicon can be engineered in a similar manner to iron by high-temperature processes. Chapter 2 contains important background information regarding minority carrier lifetime measurements, the nature of impurities in silicon, and impurity detection techniques. In Chapters 3 and 4, I employ synchrotron-based X-ray

fluorescence microscopy to study chromium distributions in multicrystalline silicon in as-grown material and after phosphorous diffusion. Interstitial chromium concentration and minority carrier lifetime measurements complement quantified precipitate size and distribution to provide insight into chromium gettering kinetics and offer suggestions for minimizing the device impacts of chromium. The quantitative data provided through this work can be used to inform future studies of the gettering kinetics of Cr in silicon, assumed to be the same in both *n*- and *p*-type silicon at solar cell processing temperatures.

During the course of this research, I have learned that detecting impurities in low concentrations in photovoltaic materials is a pressing challenge to maintain the current pace of innovation. The techniques employed in this thesis are limited to precipitated metals or specific impurities in *p*-type silicon at concentrations around 10^{10} cm^{-3}. Multicrystalline silicon in industry today is well-suited to these characterization techniques due to the high dislocation density and background contamination levels; however, as the industry considers a transition to solar cells with high-purity and/or *n*-type base materials, more sophisticated characterization techniques are required. In Chapter 5, I present a concept for a new defect characterization tool that utilizes minority carrier lifetime as a response variable.

CHAPTER

2

THEORY OF IMPURITIES AND IMPURITY DETECTION

Given the importance of mitigating the detrimental impact of metal impurities, the following sections present the relevant theory regarding lifetime, impurities and impurity detection techniques. Throughout this chapter, it is assumed that the material is uniform and isotropic, that the semiconductor is non-degenerate crystalline silicon, and that measurements are taken when the sample is in thermal equilibrium. Other assumptions are stated explicitly throughout the text when required.

2.1 Carrier lifetime

Minority carrier lifetime is generally accepted as an indicator of the efficiency potential of a wafer prior to processing into a full solar cell. Above-bandgap light incident on a solar cell is absorbed to excite electron-hole pairs. After this light is absorbed, the electrons and holes must diffuse to their respective contacts (such as the fingers, bus bars, and back contacts of a typical solar cell) to generate current. Because diffusion is not instantaneous, but instead governed by the diffusion coefficient of an electron or hole at the solar cell operating temperature, the carriers must remain in an excited state for a certain amount of time to ensure collection. The carrier lifetime is a measure of the time that electrons and holes remain in this excited state. In doped bulk material, the lifetime of minority carriers (electrons in *p*-type material and holes in *n*-type material) is typically the limiting factor due to the excess of majority carriers.

Lifetime can be expressed analytically as a function of excess minority carrier density, the rate of change of the excess minority carrier density, and the generation rate [41]:

$$\tau = \frac{\Delta n}{G - {d\Delta n}/{dt}} \tag{2}$$

where G is the generation rate and Δn the excess minority carrier density in p-type material. The generation rate is defined by the number of electron-hole pairs generated by incident photons and can be expressed as follows [42]:

$$G(\lambda, x) = \alpha(\lambda) N_0 \exp(-\alpha(\lambda) x) \tag{3}$$

where α is the optical absorption coefficient as a function of photon wavelength (λ), N_0 is the number of incident photons per unit area per unit time, and x is the depth into the material. The above equation assumes that the absorption coefficient is independent of position in the material and that absorption is governed by Beer-Lambert's law. In a typical lifetime measurement, the excess carrier density is monitored as a function of time and the generation is either known, measured simultaneously, or can be ignored in the case of high lifetime.

Lifetimes are discussed in terms of the injection level, which is formally defined as the ratio of excess to equilibrium carriers [43]:

$$\text{Injection Level} = \frac{\Delta n}{n_0 + p_0} \tag{4}$$

where n_0 and p_0 are the equilibrium carrier concentrations. Low-level injection is defined as the case when the number of excess carriers is small compared to the equilibrium carrier concentrations, typically $\Delta n \approx 10^{14}$ cm^{-3} for standard solar materials with doping levels on the order of 10^{16} cm^{-3}. High level injection is the opposite case, with $\Delta n \approx 10^{18}$ cm^{-3}. In this thesis, I will discuss the absolute injection density rather than the normalized injection level. A typical solar cell such as that depicted in Figure 2 operates at maximum power point in low injection, between 10^{12} cm^{-3} and 3×10^{13} cm^{-3} according to simulations [44]. The injection level is dependent on the solar cell architecture and conversion efficiency. For example, a more advanced solar cell with carrier-selective contacts can operate closer to 5×10^{14} cm^{-3} [44].

The apparent, or measured, lifetime of any semiconductor material is the result of competing recombination mechanisms. This apparent lifetime can be expressed as a harmonic sum:

$$\tau_{\text{meas}} = \frac{1}{\tau_{\text{Rad}}} + \frac{1}{\tau_{\text{Auger}}} + \frac{1}{\tau_{\text{SRH}}} + \frac{1}{\tau_{\text{Surf}}} + \frac{1}{\tau_{\text{other}}} \tag{5}$$

The first two terms in the above equation, radiative (Rad) and Auger, correspond to what is typically classified as the intrinsic lifetime in silicon. In the case of highly doped silicon or

dominant impurity interactions, however, Auger recombination may no longer be considered an intrinsic mechanism. The third term, Shockley-Read-Hall (SRH), represents recombination through defect centers within the bandgap of the material. The fourth term is associated with recombination at the surfaces of the semiconductor. These mechanisms corresponding to the first four terms are discussed in detail in the following sections. The last term is associated with any other, unaccounted-for recombination mechanisms (*e.g.*, recombination at precipitates if not represented by the SRH statistics).

2.1.1 Radiative recombination

Radiative recombination occurs when an electron and a hole recombine band-to-band and emit a photon of equivalent energy. In an indirect bandgap semiconductor such as silicon, radiative recombination must also involve a phonon, making it less likely to occur than the other recombination mechanisms. For a sample in thermal equilibrium, the radiative lifetime can be expressed as [45]:

$$\tau_{\mathrm{Rad}} = \frac{n_0 p_0}{\mathrm{B}(T) n_{\mathrm{i}}^2 (n_0 + p_0)} \tag{6}$$

where B is the radiative recombination coefficient and n_{i} is the intrinsic carrier concentration. The radiative recombination coefficient is equal to 2×10^{-15} cm^3/s at room temperature [45]. This coefficient changes with sample temperature: as temperature increases, the coefficient decreases. An expression for B can be derived from the generalized Planck equation for spontaneous emission from band-to-band transitions as a function of temperature and photon energy [46]:

$$\mathrm{B}(\hbar\omega, T) = \frac{1}{n_i^2} \frac{(\hbar\omega)^2 \cdot n^2}{\pi^2 \hbar^3 c_0^2} \cdot \alpha_{\mathrm{BB}}(\hbar\omega, T) \cdot \exp(-\frac{\hbar\omega}{k_{\mathrm{B}} T}) \tag{7}$$

where ω is the photon frequency, n is the index of refraction, α_{BB} is the energy- and temperature-dependent band-to-band absorption coefficient, T is the sample temperature, and k_{B} is the Boltzmann constant. To obtain the B coefficient at a particular temperature, Equation (1) must be integrated over the entire spectrum. Several studies have shown this dependence experimentally. The authors of [47] fit a 5$^{\mathrm{th}}$ order polynomial to historical experimental data to allow quick extraction of the B coefficient at arbitrary sample temperatures.

2.1.2 Auger recombination

Auger recombination involves three free carriers – either two holes and one electron or two electrons and one hole. One electron-hole pair recombines band-to-band, but rather than emitting a photon, the energy associated with the transition is transferred to a third carrier that is promoted to an excited state within its original band. Traditional models for Auger recombination assume that the carriers are quasi-free and do not interact [48]–[50]; more recent models, which agree more closely with experimental data, account for interactions due to Coulombic attraction/repulsion [51], [52], phonons [53], and impurities [54]. Combining radiative and Auger recombination, the following expression is an advanced parametrization of the intrinsic lifetime in silicon [55]:

$$\tau_{\mathrm{intr,adv}} = \frac{\Delta n}{(np - n_{\mathrm{i}}^2)(2.5 \times 10^{-31} g_{\mathrm{eeh}} n_0 + 8.5 \times 10^{-32} g_{\mathrm{ehh}} p_0 + 3.0 \times 10^{-29} \Delta n^{0.92} + B_{\mathrm{rel}} B_{\mathrm{low}})} \tag{8}$$

where n_{i}, n_0, p_0, and Δn are as defined previously; n and p are the total electron and hole densities; g_{eeh} and g_{ehh} are functions of the equilibrium carrier concentrations, defined in [55]; B_{low} corresponds to the radiative recombination coefficient for lowly doped and lowly injected silicon (4.73×10^{-15} $\mathrm{cm^3 s^{-1}}$ [46]), and B_{rel} is defined according to [56]. This expression, use to calculate intrinsic lifetime throughout this thesis, accounts for Coulomb enhancements and is valid at room temperature for both p- and n-type silicon across the injection range.

2.1.3 Shockley-Read-Hall recombination

Shockley-Read-Hall (SRH) recombination occurs through a defect center located somewhere in the bandgap. As will be discussed in Section 2.2.2, SRH recombination is representative of recombination at most metal point defects in silicon. A trap, or defect center, can affect the recombination rate by capturing or emitting an electron and/or hole to or from its respective band. The formalization of the SRH lifetime is based on the statistical probabilities of the different recombination processes [14], [15]. When $\Delta n = \Delta p$ (for small defect concentrations), the SRH lifetime is defined as follows:

$$\tau_{\mathrm{SRH}} = \frac{\tau_{\mathrm{n0}}(p_0 + p_1 + \Delta n) + \tau_{\mathrm{p0}}(n_0 + n_1 + \Delta n)}{n_0 + p_0 + \Delta n} \tag{9}$$

$$\tau_{n0} = (N_t \sigma_n v_{th})^{-1};\ \tau_{p0} = \left(N_t \sigma_p v_{th}\right)^{-1} \tag{10}$$

$$n_1 = N_C \exp\left(-\frac{E_C - E_t}{k_B T}\right);\ p_1 = N_V \exp(-\frac{E_t - E_V}{k_B T}) \tag{11}$$

where τ_{n0} and τ_{p0} are termed the electron and hole capture time constants; σ_n and σ_p are capture cross-sections for electrons and holes for a particular defect; v_{th} is the thermal velocity of carriers ($\approx 1\times10^7$ cm/s for both types); N_C and N_V are the effective densities of states in the conduction and valence bands; and E_t is the energy of the defect level with respect to one of the band edges. The above expression assumes that trapping at defect centers is negligible and does not affect the lifetime (*i.e.*, $\Delta n \approx \Delta p$), the defect level is stable within the bandgap, and the impurity concentration is not so high that it affects the background doping concentration [41]. If more than one SRH defect is present, the individual SRH lifetimes are combined by harmonic sum to determine a total SRH lifetime. The SRH lifetime can also be written in terms of the ratio of electron-to-hole capture cross-sections, k. This form of the equation reduces the number of unknown fitting parameters when lifetime spectroscopy is used for defect identification.

2.1.4 Surface recombination

Surface recombination most often occurs as a result of dangling bonds at the surface of the wafer. These discontinuities may present as Shockley-Read-Hall recombination centers, but surface recombination lifetime is typically characterized in terms of the surface recombination velocities (SRV, measured in cm/s) at the front and back surfaces of the wafer. When the two SRVs are equal, an approximation for the surface lifetime is as follows [57]:

$$\tau_{surf} \approx \frac{W}{2S} + \frac{1}{D}\left(\frac{W}{\pi}\right)^2 \tag{12}$$

where S is the SRV, W is the wafer thickness, and D is the diffusivity of the minority carrier in the material.

The SRV depends, among other things, on the passivating layer material, the deposition conditions of the passivating layer, and doping type and concentration of the wafer. Aluminum oxide (AlO_x), for example, is deposited by atomic layer deposition and is known to be an effective passivating layer for p-type materials due to a fixed negative charge that repels minority carriers from the surface, resulting in an effectively low SRV due to the absence of minority carriers [58], [59]. This type of passivation mechanism is termed "field effect." A passivating

layer may also reduce the number of trap states at the surface (D_{it}) to achieve a lower SRV. This is termed "chemical" passivation. For effective passivation (low SRV), a layer should have both field effect and chemical passivation mechanisms [60].

For the purposes of this thesis, the passivation layer employed is AlO_x, with a surface recombination velocity on the order of 10 cm/s. The SRV is estimated when necessary by passivating a high quality float-zone control wafer of similar resistivity to the samples of interest. The measured lifetime of the control sample is assumed to be equivalent to the harmonic sum of the intrinsic lifetime (8) and the surface lifetime (12).

2.1.5 Contributions to measured lifetime

Figure 4 below displays the breakdown of the different lifetime mechanisms in the case of 10^{16} cm^{-3} *p*-type doping with a single Cr_i-B_s defect center with a concentration of 5×10^{10} cm^{-3} (calculated according to the SRH statistics, discussed in Section 2.1.3). The SRV (discussed in the previous section) is taken to be 10 cm/s and constant with injection level. The lowest lifetime among the different recombination mechanisms will dominate the measured lifetime. In silicon, the intrinsic mechanisms, including radiative and Auger, represent the maximum lifetime of the material. If the measured lifetime is equal to the intrinsic lifetime, no further improvements to the material can be made. To isolate a particular mechanism from the measured lifetime, the quantities of the other mechanisms must be known or negligible. In the case of highly contaminated material, for example, the SRH lifetime is typically much lower than the intrinsic lifetime or surface lifetime. The measured lifetime can be considered to be a close approximation to the SRH lifetime. The goal throughout this thesis is to extract and analyze parameters relevant to the SRH lifetime.

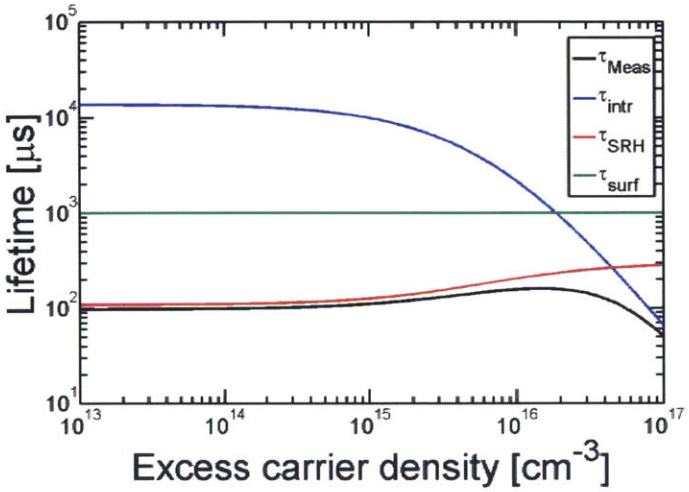

Figure 4: Breakdown of recombination mechanisms

Recombination mechanisms contribute to the overall measured lifetime of a theoretical sample. The sample has a *p*-type doping level equal to 10^{16} cm^{-3}, a concentration of Cr_i-B_s defect centers equal to 5×10^{10} cm^{-3}, and an injection-independent surface recombination velocity of 10 cm/s. In low injection, the lifetime is dominated by SRH recombination, while in high injection, the intrinsic lifetime governs the measured lifetime.

2.1.6 Lifetime measurement techniques

Common techniques used to measure carrier lifetime in silicon include photoconductance decay, free-carrier absorption, and photoluminescence. Both Sinton Instruments and Semilab offer tools to measure photoconductance decay. The Sinton Instruments WCT-120 is widely used throughout the industry and consists of a flash lamp, a calibrated light sensor, and an RF coil. The sample is placed on top of the RF coil, which measures 40 mm in diameter; when the sample is flashed with the broadband light source, excited carriers induce a voltage in the RF coil that is recorded as a function of time. The light sensor on the tool serves to measure the incident photon flux. Depending on the sample lifetime, the measurement can be performed in quasi-steady-state (QSS, $\tau < 200$ μs, $d\Delta n/dt \rightarrow 0$), transient ($\tau > 100$ μs, $G \rightarrow 0$), or generalized (any lifetime, both terms) mode. The output data consists of the apparent lifetime across the measured injection range (typically 10^{14}–10^{16} cm^{-3}). [61]

The Semilab WT-2000 performs a point-based transient lifetime measurement of microwave photoconductance decay (MW-PCD), rastered in x and y across the sample surface. Unlike the WCT-120, the WT-2000 uses a single wavelength (905 nm) to excite carriers and a microwave antenna (10 GHz) to measure reflected microwave power after excitation. The microwave power

is a function of the sample conductivity and therefore the excess carrier density. A time constant is fitted to the measured time-dependent decay curve at each (x, y) location on the sample, and a spatially resolved lifetime map is produced. While the generation rate across the sample is constant in this setup, the injection level may vary based on the underlying injection-dependent lifetime curve and must be estimated separately at each pixel. [62]

Similar to photoconductance decay, free-carrier absorption (FCA) is a transient measurement of the time-dependent carrier density in the material after an excitation pulse. In an FCA measurement, carriers are pumped into the material with a laser pulse greater than or equal to the bandgap of the material (1.124 eV for silicon) while transmission of a continuous wave probe beam with an energy much less than that of the bandgap is measured as a function of time. Carriers that are already in an excited state in either the valence or conduction band will readily absorb low-energy light. The FCA coefficient is proportional to the excess carrier density. Assuming uniform generation throughout the sample thickness, Beer-Lambert's law can be used to relate the transmitted light intensity to excess carrier density and eventually to lifetime. Like the WCT-120, FCA provides injection-dependent lifetime data. Though it is a point-based measurement, the technique can be implemented with a rastering mechanism to produce spatially resolved information. [63]

Photoluminescence (PL) can be performed as a transient pump-probe optical measurement (similar to FCA) or as a QSS measurement using a CCD camera. In the transient approach, carriers are pumped into an excited state and the lifetime is measured according to the intensity of the luminescence signal that corresponds to the amount of radiative recombination occurring in the material. In the QSS approach, widely used for silicon lifetime measurements, the sample is uniformly illuminated with a single wavelength above the bandgap of the material while a CCD camera captures luminescent photons as a function of spatial position. The measured luminescence intensity must be calibrated to the excess carrier density or the lifetime of the material. Several methods, including calibration by photoconductance [64] and self-consistent calibration with a specialized detector [65], have been defined to convert the luminescence intensity to lifetime for the QSS measurement. As with MW-PCD, the generation rate across the sample is constant while the measured injection level may vary. To specify the entire injection-dependent lifetime curve, images must be taken at a range of different illumination laser powers and then stitched together pixel-by-pixel.

2.2 Metallic impurities

Metal impurity contamination of solar cells can occur at any point throughout the manufacturing process, but contamination is most likely to occur during high temperature steps (*e.g.*, during crystal growth) when impurities are highly mobile. Transition metals are known to form mid-gap levels within the bandgap of silicon, affecting bulk lifetimes at low concentrations. The diffusion length of an impurity is related to its diffusivity and the duration of the high temperature step as follows [66]:

$$L = \sqrt{\mathrm{D}(T)t} \tag{13}$$

where L is the diffusion length, D is the temperature-dependent diffusivity of the impurity, and t is the duration. Given a sufficient surface contamination on a wafer, for example, the affected volume of material is related to the diffusion length during processing. As explained in [66], three cases are possible given a high concentration of mobile impurities: 1) Precipitates of impurity atoms form within the bulk; 2) Precipitates of impurity atoms form near the wafer surface; or 3) Impurity atoms remain in dissolved form throughout the material. In the following sections, I will discuss cases (1) and (3), which are most common for transition metal impurities.

2.2.1 Precipitated metals

Precipitate nucleation can occur homogeneously (*i.e.*, throughout a single crystalline material) or heterogeneously at structural defects. In as-grown multicrystalline material, it has been shown experimentally that metal precipitate nucleation is favored at bulk heterogeneous nucleation sites [9], [67], [68]. Metal precipitation occurs at a certain critical level of impurity super-saturation, which is a function of temperature, concentration, solubility, diffusivity, nucleation site density, and nucleation energy barrier [66], [69]. The solubility and diffusivity of a particular impurity are functions of temperature [66]:

$$S = S_0 \exp\left(\frac{S_\mathrm{S}}{k_\mathrm{B}} - \frac{H_\mathrm{S}}{k_\mathrm{B}T}\right) \tag{14}$$

$$D = D_0 \exp\left(-\frac{H_\mathrm{M}}{k_\mathrm{B}T}\right) \tag{15}$$

where S_0 and D_0 are temperature-independent coefficients, S_S is the solution entropy, H_S is the solution enthalpy, and H_M is the migration enthalpy. With knowledge of precipitation kinetics,

precipitate size and distribution can be engineered through design of time-temperature profiles for phosphorous diffusion gettering (Section 2.4).

Since precipitates tend to be located at structural defects such as grain boundaries, it is difficult to separate the effects of the different mechanisms on minority carrier lifetime or diffusion length. With careful sample preparation, the authors of [70] were able to form $NiSi_2$ precipitates without other defects and fit their results with an α coefficient of 0.7 to the following equation for the carrier diffusion length:

$$L_D = \alpha N^{-1/3} \tag{16}$$

where α is a constant that depends on the specific defect and N is the defect concentration. An alternative approach defines the lifetime due to metal precipitates to be a form of the SRH equations under low injection, where the capture cross-section, concentration, and thermal velocity of the defect are related to the spherical precipitate size and density (r, N), the recombination velocity at the precipitate surface (s), and the minority carrier diffusion length (D) [20], [71]:

$$\frac{1}{\tau_{prec}} = 4\pi r^2 N \frac{sD/r}{s + D/r} \tag{17}$$

A Schottky effect model has been proposed to further refine the description of recombination at metal precipitates by accounting for band-bending at the precipitate surface [72]. Precipitate recombination is an area of ongoing research and is not the subject of this thesis. This thesis focuses on recombination at metal point defects (next section), but it is important to recognize that precipitated metals can also contribute to the total recombination rate in the material.

2.2.2 Metal point defects

Metal point defects can be either interstitial (between lattice sites) or substitutional (sitting on a lattice site). Dopant atoms, for example, are a form of substitutional impurity that sits directly on a silicon lattice site. The material's resistivity is decreased by their addition because the dopant atoms typically have one less or one more electron than a silicon atom. The energy levels of phosphorous and boron, common dopant impurities, lie very close to the conduction and valence bands, respectively, so that they are easily ionized at room temperature. Metal impurities, when present in concentrations on the order of the dopant concentration, can contribute in a similar way to the intrinsic carrier concentration. In industrial materials, this is

typically not the case as dopant levels for photovoltaic materials are $\approx 10^{16}$ cm^{-3} while impurity levels are 10^{14} cm^{-3} or less.

A metal point defect can be uniquely characterized by its energy level with respect to one of the band edges and its capture cross-sections for electrons and holes. Recombination at transition metal point defects can then be modeled by the SRH statistics, as explained in Section 2.1.3. Common metal impurities that limit performance in photovoltaic materials include iron (Fe), chromium (Cr), copper (Cu), and nickel (Ni). The effect of these impurities on solar cell performance has been studied both experimentally [16], [25] and through simulation [17], [18].

2.2.3 Chromium

Chromium (Cr) is known to be a detrimental impurity in silicon, affecting solar cell performance at concentrations as low as 10^{10} cm^{-3} [16]–[18]. In interstitial form, chromium acts as a highly effective recombination center in both *p*- and *n*-type silicon. Compared with iron, the minority carrier capture cross-sections for chromium are 1.5 and 57 times larger in *p*- and *n*-type silicon, respectively. Interstitial chromium (Cr_i) forms at donor level at 0.24 eV below the conduction band, with a capture cross-section for holes of 4×10^{-15} cm^2 and a capture cross-section for electrons of 2×10^{-14} cm^2 [30]. In *p*-type materials, Cr_i forms a metastable pair with substitutional boron (B_s). At room temperature, Cr_i donates its electron to the conduction band to become positively charged, while B_s accepts an electron to become negatively charged. Coulombic attraction causes a defect complex (Cr_i-B_s) to form which is dominant under standard solar cell operating conditions. The Cr_i-B_s formation and dissociation kinetics equations are not reproduced here but explained by Equations (1)–(10) in [30]. Cr_i-B_s forms a donor level at 0.27 eV above the valence band with a capture cross-section for holes of 1×10^{-14} cm^2 and a capture cross-section for electrons of 2×10^{-14} cm^2 [30]. Chromium also forms precipitates in silicon and has previously been observed by energy dispersive X-ray spectroscopy to form chromium disilicide ($CrSi_2$) [34]. This spherical precipitate consists of three Cr atoms in a hexagonal configuration with a unit cell volume of 3.61×10^{-23} cm^3 [73], [74].

2.2.4 Iron

Iron (Fe) is another important impurity in crystalline silicon whose kinetics have been relatively well-studied. Interstitial iron (Fe_i) forms a donor level located 0.38 eV above the

valence band, with a capture cross-section for holes of 7×10^{-17} cm^2 and a capture cross-section for electrons of 1.3×10^{-14} cm^2 [8], [18], [75]. The resulting defect level is highly asymmetric, with a k value of 185. Similar to chromium, Fe_i forms a metastable pair with B_s. Upon illumination or heating, Fe_i and B_s are separated; left in the dark at room temperature, the two atoms will form Fe_i-B_s. Details regarding preparation of the two states can be found in [32], [75], [76]. Fe_i-B_s forms a donor level at 0.26 eV below the conduction band, with a capture cross-section for holes of 3×10^{-15} cm^2 and a capture cross-section for electrons of 5×10^{-15} cm^2 [18], [77]. Iron forms spherical iron-silicide precipitates ($FeSi_2$) with unit cell volume equal to 3.76×10^{-23} cm^3 [78].

2.3 Impurity detection techniques

It is important to be able to detect and characterize defects in solar cell materials to design mitigation steps such as phosphorous diffusion gettering (Section 2.4). In general, the goal is to identify the defects in a non-contact, non-destructive manner such that the response of the defect to different processes can be studied, that a solar cell could be made from the material, or even that the measurement could be performed in-line during manufacturing. Destructive techniques exist which work well to identify defects when present in high concentrations, including Inductively-Coupled Plasma Mass Spectrometry (ICPMS) and Secondary Ion Mass Spectrometry (SIMS). Electrical techniques such as Electron Beam-Induced Current (EBIC) and Deep-Level Transient Spectroscopy (DLTS) require the formation of a diode on the sample surface and can be complicated in analysis.

2.3.1 Micro-X-ray fluorescence

Synchrotron-based X-ray fluorescence (μ-XRF) is a non-destructive technique that has proven useful to probe transition metal precipitate distributions in silicon [9], [21], [67], [68]. The measurement involves high energy X-rays that excite core shell electrons in the sample material. As these excited electrons relax back to their resting states, corresponding photons are emitted and measured by a detector. The emitted fluorescence as a function of energy forms a spectrum that can be analyzed for chemical composition. In the studies presented in this thesis, the measured fluorescence corresponds to the K_α transition of the impurity. When XRF is implemented at a synchrotron with an x-y positioning stage, high-resolution spatially resolved

maps of chemical composition can be produced. Elemental detection depends on the absorption and fluorescence edges relative to the incident beam and detector capabilities. The beam energy used for this thesis is 10 keV, so that any element with an absorption edge at or below that energy can theoretically be detected.

For each sample measured at the beamline, long-duration, single-point μ-XRF measurements of NIST standard reference materials 1832 and 1833 are used to quantify the background level. The minimum detection limit (MDL) of the technique is calculated according to the following equation, based on [67]:

$$\mathrm{MDL} = \frac{3\sqrt{I_{\mathrm{Bkgd}}}}{I_{\mathrm{Std}}} \times \rho_{\mathrm{Element,Std}} \times A \times \sqrt{t} \tag{18}$$

where MDL is measured in detectable grams for a particular element, $\rho_{\mathrm{Element,Std}}$ is the areal density of the element of interest in the NIST standard reference material (g/cm^2), A is the full-width half-maximum beam spot size (cm^2), and t is the actual measurement time for the standard material. The I_{Bkgd} and I_{Std} terms correspond to the background or noise-related fluorescence and fluorescence from the standard reference material. These terms are calculated by fitting the fluorescence energy spectrum and calculating the area under the curve associated with the element of interest. The quantity $3\sqrt{I_{\mathrm{Bkgd}}}$ represents the estimated noise level of the measurement. A similar equation is used to quantify spatially resolved μ-XRF maps, with the background term replaced by the measured fluorescence at a particular pixel.

An example of a fluorescence spectrum from the 1832 reference material is shown in Figure 5. The table on the right in the figure lists the elements that are included in 1832. Reference material 1833 contains Si, K, Ti, Fe, Zn, and Pb. The elements in the standards represent most elements of interest for silicon solar cell contamination. For elements that are not included, such as chromium, the MDL can be interpolated from measurements of the nearest elements on the periodic table. For chromium, these elements are vanadium (V) and manganese (Mn).

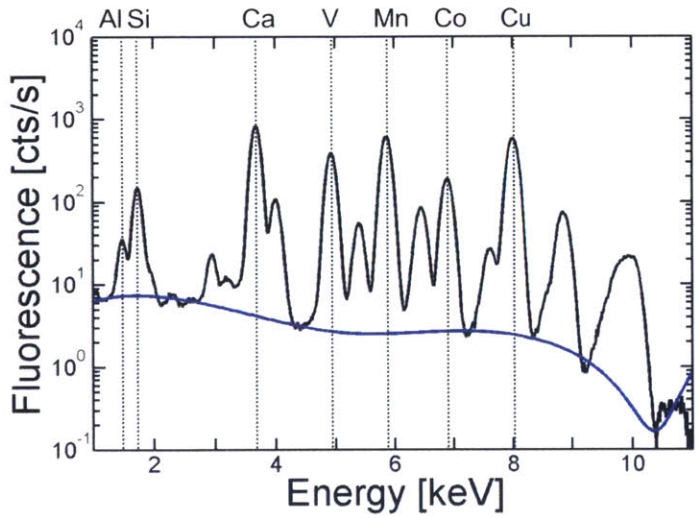

NIST Standard Reference Material 1832			
Element	K_α	K_β	Areal density
-	eV	eV	μg/cm^2
Al	1486.7	1557.45	13.7
Si	1739.7	1835.94	33
Ca	3691.68	4012.7	18.5
V	4952.2	5427.29	4.2
Mn	5898.75	6490.45	4.2
Co	6930.32	7649.43	0.9
Cu	8047.78	8905.29	2.2

Figure 5: Fluorescence energy spectrum of NIST standard reference material 1832

A sample fluorescence spectrum from NIST standard reference material 1832 is shown (left). The blue solid line is an example of a fitted background curve. The vertical dotted lines correspond to the K_α fluorescence energy for each of the elements included in the standard. The MDL is calculated by estimating the area under the plotted curve for a particular element. The fluorescence energies and areal densities for the standard reference material are shown in the table (right).

The minimum detection limit in grams is converted to detectable Cr atoms according to the following equation:

$$\frac{\text{atoms}}{\text{precipitate}} = \frac{\text{MDL [g]}}{\text{Atomic weight Cr } [\frac{\text{g}}{\text{mol}}]} \times N_{\text{Av}}[\frac{\text{atoms}}{\text{mol}}] \tag{19}$$

where N_{Av} is Avogadro's number.

2.3.2 Metastable defect lifetime spectroscopy

Another group of techniques that will be employed throughout this thesis is based on extracting and analyzing the SRH lifetime of a given material. As mentioned in Section 2.2.3, chromium forms a metastable defect complex with substitutional boron in *p*-type silicon. Similarly, both iron and oxygen form metastable defect complexes in *p*-type silicon. With knowledge of the formation kinetics and defect parameters of these complexes, lifetime measurements in the associated and dissociated states can be used to extract the chromium, iron, and/or oxygen concentration in the material [27], [30], [32], [75], [76], [79]. If the two states are not fully isolated (*i.e.*, if State 1 consists of a small fraction of Cr_i-B_s and a large fraction of Cr_i

and State 2 consists of a large fraction of Cr_i-B_s and a small fraction of Cr_i), the following series of equations can be used to determine the concentration of the defect N of interest:

$$[N] = \mathrm{C}(\Delta n)\left[\frac{1}{\tau_1} - \frac{1}{\tau_2}\right] \tag{20}$$

$$\mathrm{C}(\Delta n) = \frac{1}{f_1 \chi_1^{\mathrm{N-B}} + (1 - f_1)\chi_1^{\mathrm{N}} - f_2 \chi_2^{\mathrm{N}} - (1 - f_2)\chi_2^{\mathrm{N-B}}} \tag{21}$$

$$\chi_{1,2}^{\mathrm{N,N-B}} = \frac{v_{\mathrm{th}} \sigma_{\mathrm{n}} (N_{\mathrm{A}} + N_{\mathrm{D}} + \Delta n)}{N_{\mathrm{A}} + p_1 + \Delta n + k(N_{\mathrm{D}} + n_1 + \Delta n)} \tag{22}$$

where f_1 and f_2 relate to the fraction of N_i or N_i-B_s in either state, χ is derived from the SRH lifetime equations for the particular defect, N_A and N_D are the acceptor and donor dopant concentrations, and all other parameters have been previously defined. The exact formation of Equations (20)–(22) depends on the injection level of the measurement and the relative lifetimes of the defects at that injection level. For example, in low-level injection, the SRH lifetime due to Fe_i-B_s pairs is higher than the SRH lifetime due to Fe_i point defects, so that τ_1 would correspond to Fe_i and τ_2 to Fe_i-B_s. In high-level injection, the lifetime trend is switched. The detection limit for such a technique can be as low as 10^9 cm^{-3}, but this is dependent on the injection level, lifetime, defect, and precision of the lifetime measurement. To produce a reliable measurement, the defect states must be controlled so that the fraction of each defect in States 1 and 2 is known with high precision.

2.3.3 Generalized lifetime spectroscopy

Lifetime spectroscopy can also be applied more generally to silicon materials for defect identification. Given an injection-dependent lifetime curve, the SRH lifetime can be extracted with knowledge of the intrinsic and surface lifetime components, as explained previously. Each defect, characterized by its concentration, energy level and capture cross-sections, presents a unique signature in terms of the SRH lifetime magnitude and injection-dependent shape. One approach to extracting the defect parameters from an injection-dependent curve is linearizing the SRH equation [80]:

$$\tau_{\mathrm{n}} = \frac{1}{\alpha_{\mathrm{n}} N_{\mathrm{t}}}\left[1 + \frac{Q n_1}{p_0} + \frac{p_1}{p_0} + X\left(Q - \frac{Q n_1}{p_0} - \frac{p_1}{p_0}\right)\right] \tag{23}$$

where α_n is the electron capture coefficient of the defect ($\sigma_n \times v_{th}$ from the SRH lifetime), Q is the ratio of electron capture coefficient to hole capture coefficient, and X is a revised independent

parameter ($X = n/(p_0 + n)$). Equation (23) is written for the case with one dominant defect in p-type material, but similar equations can be written for multiple defects and for n-type material. A set of experimental SRH lifetime data is plotted versus the normalized injection level X to reveal the nature of the defect or defects. If one defect is dominant, the plot will show a linear line with a slope and intercepts that are related to that defect. If multiple defects are dominant, the plot will exhibit some curvature or a slope that relates to the harmonic sum of the two defects. An example of this linearization in the case of simulated SRH lifetimes is shown in Figure 6 below. The defect parameters are extracted by analyzing the slope and intercepts of the linear line or linear fits to the curve in the case of multiple defects, as explained in detail in [80].

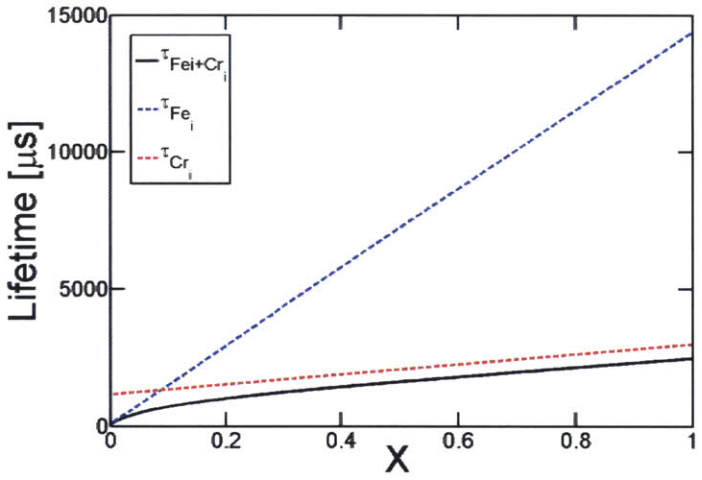

Figure 6: Shockley-Read-Hall linearization for defect analysis

The linearized SRH lifetime is plotted for a p-type sample with 10^{10} cm^{-3} Cr_i and 10^{11} cm^{-3} Fe_i. The y-axis of the graph is the lifetime, while the x-axis is the normalized injection level defined in the text. The doping level of the sample is 10^{16} cm^{-3}. The overall lifetime curve (black solid line) has a slight curvature with respect to the x-axis, which indicates the presence of two lifetime-limiting defects. If the sample contained only Cr_i or only Fe_i, the lifetime curve would be linear as shown by the red and blue dashed lines, respectively.

Extensions of lifetime spectroscopy involve analyzing the temperature and doping dependence of the lifetime either simultaneously or in addition to the injection-dependent analysis. Temperature-dependent lifetime spectroscopy (TDLS) measures the low-level injection lifetime as a function of temperature. In low-level injection (LLI), as was shown qualitatively in Figure 4, the measured lifetime is typically dominated by SRH recombination if a defect is present. The measured lifetime is therefore taken to be the SRH lifetime; if this assumption is not

valid for a particular sample, extraction of the SRH lifetime can be performed as explained previously with knowledge of the other recombination mechanisms. The temperature-dependent LLI lifetime is then plotted on an Arrhenius plot ($\log(\tau_{LLI}/T)$ v. $1000/T$). The slope of the linear increase of the plotted curve is equal to the defect energy depth; a fit to the entire curve, including the linear increase and some non-linear portion of the curve, yields the bandgap half. [41]

Doping-dependent lifetime spectroscopy (N_{dop}-IDLS) and temperature- and injection-dependent lifetime spectroscopy (TIDLS) are more advanced approaches to probing the defect parameters. The SRH lifetime is measured at either different doping levels or different temperatures, both of which affect the SRH formalization (9) in known and predictable ways. By fitting each injection-dependent curve independently for the defect parameters and then analyzing the trends across doping level or temperature, the defect can be specified unambiguously in terms of E_t, k (the ratio of capture cross sections), and τ_{n0} or τ_{p0} (10). The challenge of implementing N_{dop}-IDLS is sample fabrication. For robust analysis, the defect population between samples must be identical while only the doping level is varied. This is difficult unless, for example, the doped wafers can be grown directly from the melt or from gas and process conditions can be closely controlled. TIDLS and its practical application will be discussed in more detail in Chapter 5. [41]

2.4 Impurity gettering by phosphorous diffusion

Gettering is a method of engineering the distribution of metal impurities to improve solar cell performance. Graff defined gettering to be a temperature-dependent process in which "unwanted metal impurities" are redistributed such that their impacts on device performance are minimized [66]. In this thesis, I will focus on gettering during phosphorous diffusion, a process step used to form the highly doped *n*-type emitter layer of a diffused junction *p*-type silicon solar cell. The high temperatures and times required during phosphorous diffusion compared to other solar cell processing steps provide an opportunity to manipulate and redistribute metal impurities as Graff suggests. Phosphorous diffusion gettering (PDG) has also been shown to be effective for *n*-type materials, improving lifetime over two orders of magnitude [81].

A typical PDG process consists of three steps, as depicted in Figure 7. In the first step (heating), the samples are loaded in the furnace and the temperature is increased to the plateau

temperature. In the second step (plateau), phosphorous is deposited on the sample surface. In the case of $POCl_3$ diffusion by tube furnace, this step occurs at a high temperature with $POCl_3$ gas bombarding the sample. During the plateau, deposited phosphorous is driven into the sample to produce the desired phosphorous concentration profile. In the third step, the sample can be unloaded directly at the plateau temperature, cooled to a specified unloading temperature and then cooled in ambient conditions to room temperature, or a low-temperature extended anneal can be performed before unloading. The exact design of the time-temperature profile depends on goal of the process, the equipment, and the capability to achieve a given temperature or cooling rate.

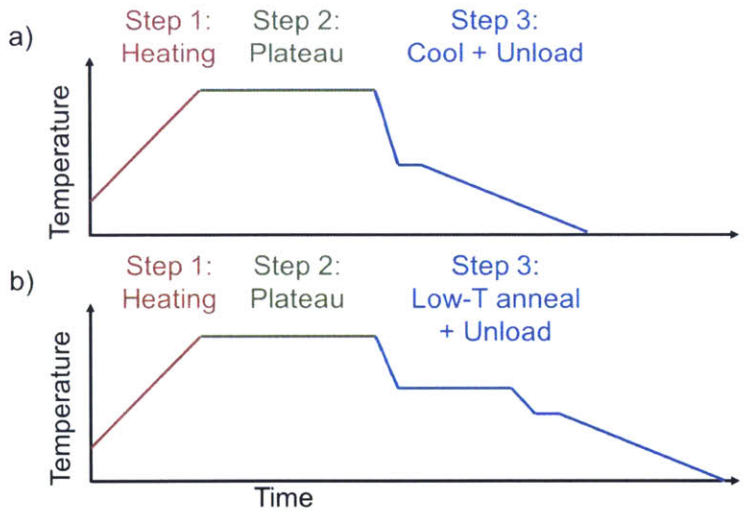

Figure 7: Sample phosphorous diffusion gettering time-temperature profiles

Three generic process steps are depicted that result in the formation of a phosphorous-rich layer at the sample surface. a) A standard PDG time-temperature profile with a rapid cooldown followed by immediate unloading. b) An advanced PDG time-temperature profile with an extended low-temperature anneal following by unloading. The exact profile will depend on the goal of the process and the equipment capabilities.

The time-temperature diffusion profile is correlated to the evolution of metal precipitates and point defects. In general, metal precipitates are dissolved during step 2 that occurs at high temperature. This dissolution process is governed by the solubility of the particular defect and diffusion due to concentration gradients in the material at a given temperature. As the phosphorous-rich layer grows, metal point defects will segregate to the emitter, driven by a difference in solubility between the bulk and emitter. As temperature decreases, the ratio of the

emitter to bulk solubility (termed the "segregation coefficient) increases [19]. In other words, the driving force for impurity migration to the emitter is greater at lower temperatures. This segregation and agglomeration of point defects in near-surface regions is termed "external" gettering. The low-temperature anneal is typically intended to aid in external gettering by providing sufficient time and temperature for complete diffusion and segregation to occur. During cooling, the metal point defects that have not externally gettered will be redistributed to precipitates due to the decreasing solubility or "frozen" in point-defect form due to a low diffusivity combined with a lack of nearby precipitates or nucleation sites. This redistribution to precipitates or nucleation sites is termed "internal" gettering. The mechanisms behind PDG are complex and require solution of multi-dimensional partial differential equations to understand the exact response of metal impurities to a given time-temperature profile. For this reason, many researchers have devoted their efforts to developing models of the PDG process to provide insight into this behavior [19], [20], [23], [38], [82]–[84].

CHAPTER

3

SAMPLE PREPARATION

To study the gettering kinetics of chromium in silicon, a representative sample set was selected and processed by phosphorous diffusion. This section presents the sample details, treatments applied, and measurement methods. Portions of this section are based on [85], a manuscript submitted and accepted for publication.

3.1 Sample description

Two adjacent (sister) wafers were selected from a 12 kg laboratory-scale intentionally chromium-contaminated multicrystalline silicon (mc-Si) ingot (Figure 8) [25]. These wafers were taken from 83% ingot height. From B and Cr concentrations of 0.34 ppma and 108 ppma added to the melt, I estimate a *p*-type B doping concentration of 1.94×10^{16} cm^{-3} and a Cr concentration of 9.85×10^{13} cm^{-3} using the Scheil equation [86], [87]:

$$C_s = k_{eff} C_0 (1 - f_s)^{k_{eff}-1} \quad (24)$$

where C_s is the concentration of the impurity in the wafer, C_0 is the initial melt concentration, f_s is the solidified fraction or ingot height, and k_{eff} is the effective segregation coefficient. Segregation coefficients for B and Cr were taken to be 0.8 [87] and 3.1×10^{-6} [25], respectively. The estimated B concentration is consistent with four-point probe and Sinton Instruments WCT-120 measurements.

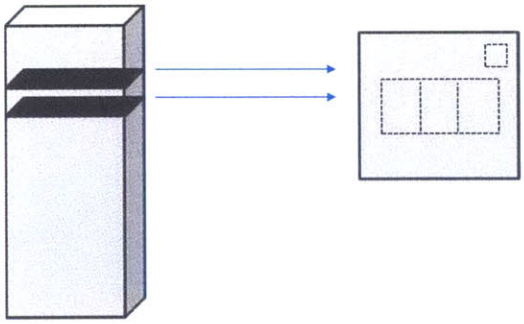

Figure 8: Chromium-contaminated sample selection

Two adjacent wafers were selected from the top half of an intentionally-contaminated multicrystalline silicon ingot. From each wafer, one small sample was cut for μ-XRF measurements at the Advanced Photon Source and three larger samples were cut for lifetime spectroscopy measurements.

3.2 Sample treatment

For synchrotron-based micro-X-ray fluorescence measurements, 1-cm^2 samples were cut from vertically adjacent locations in the wafers (Figure 8). Electron backscatter diffraction (EBSD) was used to identify a random angle grain boundary (35.3°) common to both samples for analysis. Prior to measurements, the as-grown samples were saw-damage etched (CP4) and RCA-cleaned; for post-gettering measurements, the phosphorous silicate glass (PSG) layer was etched with HF and samples were RCA-cleaned, leaving the phosphorous-doped emitter layer intact.

Three 5 × 4 cm^2 samples were cut from each sister wafer (Figure 8) for lifetime and chromium point-defect concentration measurements. After saw-damage (as-grown) and emitter (post-gettering) removal by CP4 followed by RCA cleaning, a 20 nm passivating layer of Al_2O_3 was deposited on both sides of the samples by atomic layer deposition (ALD) at 200°C (Cambridge NanoTech Savannah 200) followed by a 12-minute anneal in a N_2 ambient at 350°C. All lifetime and chromium point-defect concentration measurements were performed in the passivated state.

The samples were subjected to phosphorous diffusion gettering in a $POCl_3$ tube furnace (Tystar Titan 3800). The samples from the first sister wafer received a standard diffusion (STD): annealed at 845°C for 25 min and unloaded directly at 845°C. The samples from the second sister wafer received a high-temperature extended diffusion (EXT): annealed at 920°C for 76 min, and cooled to 600°C for an additional 60 min anneal before unloading. The EXT process

was chosen due to its enhanced iron gettering efficiency compared to the STD process [22]. The two time-temperature profiles were measured by three thermocouples located inside the tube furnace (load, center, and source), shown in Figure 9.

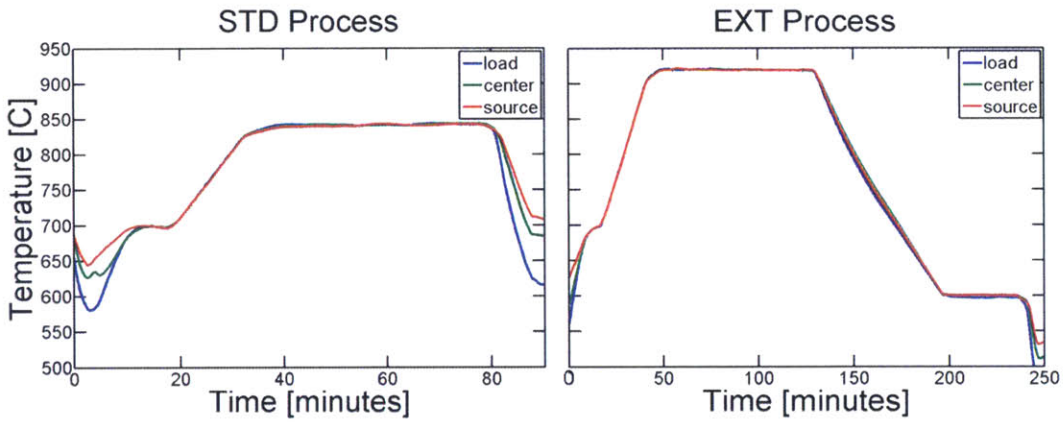

Figure 9: Phosphorous diffusion gettering time-temperature profiles for chromium samples

Time-temperature profiles as measured during diffusion of chromium-contaminated samples. The STD process (left) consists of a lower diffusion temperature and shorter hold time, while the EXT process (right) achieves a higher diffusion temperature and incorporates a low-temperature anneal.

3.3 Measurements performed

In each state (as-grown and post-gettering), spatially resolved μ-XRF measurements intended to probe the chromium precipitate size and distribution were taken in the same location along at least 20 μm of the aforementioned grain boundary, with a step size of 220 nm and a full-width half-maximum beam spot size of approximately 200 nm. μ-XRF measurements were conducted at the Advanced Photon Source Beamline 2-ID-D at Argonne National Laboratory [88]. μ-XRF data analysis assumes a spherical $CrSi_2$ precipitate with a unit cell volume of 3.61×10^{-23} cm^3 [73], [74]. The μ-XRF measurement and analysis procedure is outlined in detail in [21]; a noise cutoff of 4 standard deviations was used to process the data presented herein.

To provide further insight into chromium gettering kinetics, lifetime and chromium point-defect concentration measurements were also performed before and after each process. Spatially resolved lifetime and chromium point-defect concentrations (post-gettering) were measured by performing a series of photoconductance-calibrated photoluminescence (PC-PL) measurements in isolated defect states, as described in [30] and [76]. First, the sample was heated in the dark at

250°C for 10 minutes and then illuminated at room temperature for one minute with an 808 nm diode laser (Lumics, 25 W, operated at 70% power, ≈0.25 suns) to dissociate iron-boron (Fe_i-B_s) pairs just before a lifetime measurement was performed (Cr_i, Fe_i, and BO-complex largely deactivated). A second thermal dissociation at 250°C in the dark for 10 minutes was applied before storing in the dark at 70°C for 5 hours. Thereafter, the sample was illuminated for one minute to dissociate Fe_i-B_s pairs and the second lifetime measurement was performed (Cr_i-B_s, Fe_i, and BO-complex largely deactivated). Equations (1)–(10) and SRH defect parameters (reproduced in Section 2.2.3) reported in [30] were used to calculate interstitial chromium concentration. Average lifetime and chromium point-defect concentrations (as-grown and post-gettering) were also measured in a similar manner with a Sinton Instruments WCT-120.

A similar process to that described above was used to perform measurements of iron point-defect concentrations with PC-PL. The sample was illuminated with the 808 nm laser (70% power, ≈0.25 suns) to dissociate Fe_i-B_s pairs. After illumination, the sample was left in the dark at room temperature for two hours. The first lifetime measurement was then performed (Fe_i-B_s) with a low intensity illumination and an exposure time of 10 seconds to minimize Fe_i-B_s pair dissociation during the measurement. The sample was illuminated to intentionally dissociate the pairs just before the second lifetime measurement was performed (Fe_i) with the same image settings. Calculation of [Fe_i] assumes that the associated state consists of 99% Fe_i-B_s pairs, and the dissociated state consists of 99% Fe_i [79]. The Fe_i-B_s pair association and dissociation steps do not result in significant changes in the Cr_i and Cr_i-B_s populations; to minimize errors, iron point-defect measurements were performed after a five-hour Cr_i-B_s association anneal. The BO-complex is affected by illumination, but the timescale for defect formation is much longer than that of Fe_i-B_s pairs [76]. Lifetime measurements taken before and after each illumination were compared to confirm that BO-complex formation does not affect the iron point-defect measurements for these samples.

All PL measurements were performed using the 808 nm diode laser and a Princeton Instruments PIXIS 1024BR camera, fitted with an InP wafer and a Schott RG1000 long-pass filter. The WCT-120 was used to calibrate the PL images according to [64]. A Czochralski silicon sample of similar thickness, reflectivity, and resistivity was used to determine the calibration parameters. I corrected the second fit parameter (b in $y = ax^2 + bx$), proportional to the doping concentration of the sample [64], to match the chromium sample doping

concentration. The PL measurement variation is 4.4%, estimated by imaging the Czochralski sample 15 times while illuminated under similar conditions. 50 points on the sample were analyzed, including both low and high lifetime areas. The PL image of the sample and a plot from a representative point are shown in Figure 10.

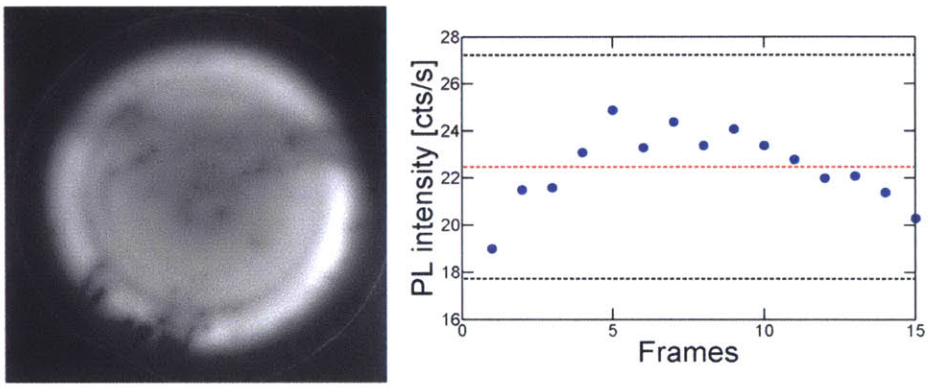

Figure 10: Photoluminescence variation measurements

PL images of a Czochralski sample (left) were used to estimate the measurement variation. 15 frames, or images, were taken of the illuminated sample. 50 points on the sample were analyzed for mean and standard deviation, as shown on the right for a representative pixel. The red dotted line represents the mean, while the black dotted lines represent 3 standard deviations from the mean.

The detection limit ($\approx 5\times10^{9}$ cm^{-3} in the highest lifetime areas of the chromium-contaminated samples) is estimated pixel-by-pixel by propagating this 4.4% variation through the $[Cr_i]$ calculation as follows:

$$s_{Cr_i} = \sqrt{\left(-\frac{C}{{\tau_{Cri}}^2} s_{\tau Cr_i}\right)^2 + \left(\frac{C}{{\tau_{Cr_B}}^2} s_{\tau Cr_B}\right)^2} \tag{25}$$

$$S_\tau = \frac{\partial \tau}{\partial PL} s_{PL} = \left(\frac{1}{G}\right)\left(\frac{\partial n}{\partial PL}\right)\left(\frac{\%}{100} \times PL\right) \tag{26}$$

$$\frac{\partial n}{\partial PL} = \left(b^2 - 4a(c - PL)\right)^{-1/2} \tag{27}$$

where C is the matrix used to calculate the impurity concentration as described by Equations (20)–(22), PL is the measurement variation in percent, G is the generation rate as measured by a silicon photodiode, and a, b, and c are the fit parameters associated with the lifetime calibration.

CHAPTER

4

PHOSPHOROUS DIFFUSION GETTERING RESPONSE

This section describes the evolution of precipitated and interstitial chromium after gettering and offers insight into time-temperature profile design. Portions of this section are based on [85], a manuscript accepted for publication.

4.1 Detecting and gettering precipitated chromium

In the as-grown state, chromium precipitates were detected by μ-XRF along the random-angle grain boundary identified by EBSD (Figure 11), consistent with the behavior of other metals in silicon wherein metal precipitate nucleation is favored at bulk heterogeneous nucleation sites [9], [67], [68]. A total of 18 precipitates were measured with a precipitate line density of 0.42 precipitates/μm. The Cr-rich precipitates in the as-grown material were found to be coincident with copper-rich particles, as indicated by the fluorescence spectrum (Figure 12). Cr-rich precipitates were observed to be smaller on average compared to iron-rich precipitates formed under similar crystallization conditions in another ingot. In the iron-contaminated material presented in [21] ([Fe] = 5.05×10^{14} cm^{-3}), a total of 30 iron-rich precipitates were identified, with a line density along a Σ3 grain boundary equal to 1.27 precipitates/μm.

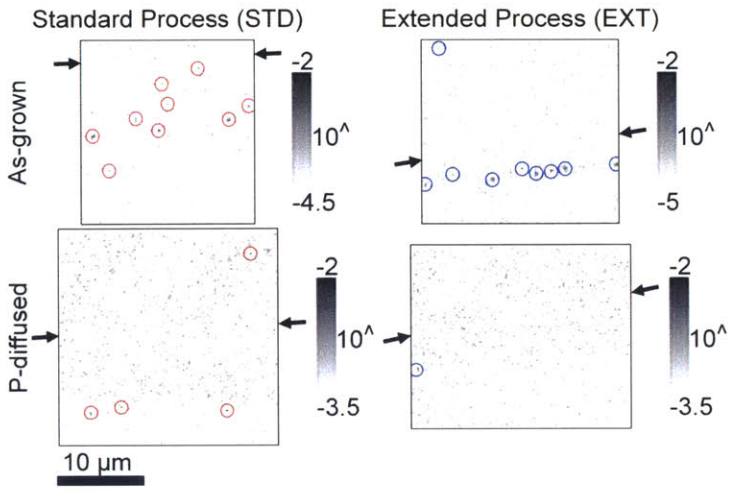

Figure 11: μ-XRF measurements along random-angle grain boundary

In each spatially resolved map, the pixel intensity is determined by the fluorescence associated with chromium, measured in $\mu g/cm^2$ with a logarithmic scale. Precipitates identified to be above the estimated noise floor are circled in red (STD) and blue (EXT). These images have been cropped for display, while the analysis in Figure 13 has been performed on the full data set. Black arrows indicate where the grain boundary line (visible from elastically scattered X-rays, not shown) enters and exits the map.

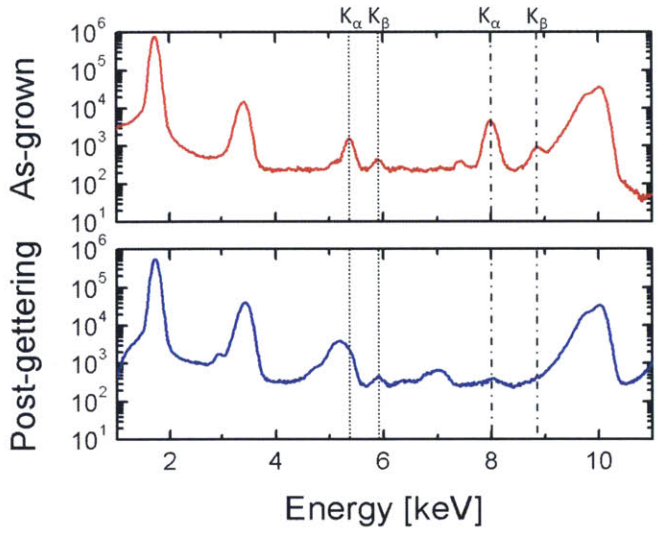

Figure 12: Fluorescence spectra at metal-rich particles

Fluorescence energy spectra (measured in counts) at metal-rich particles in the as-grown (top) and post-gettering states (bottom). In both states, fluorescence associated with the chromium K_α and K_β (vertical dotted lines) is present. Post-gettering, there is very little fluorescence associated with the copper K_α and K_β (dash-dotted lines). The fluorescence measured near the chromium K_α is due to the third harmonic of silicon and is accounted for in the analysis.

The iron and chromium as-grown precipitate size distributions are compared in Figure 13. The noise floors, represented by the gray "+" for each distribution, are similar in magnitude. Due to the high detection limits, the precipitate distributions cannot be fully specified by μ-XRF data [89]. No chromium precipitate larger than 3.6×10^5 Cr atoms/precipitate is detected, while the maximum iron precipitate size is nearly one order of magnitude larger, 2.9×10^6 Fe atoms/precipitate. Similar differences in precipitate size after crystallization were predicted through simulation by Schön *et al.* [35]. The authors attributed the tendency toward smaller chromium precipitates to a lower diffusivity of chromium compared to iron. These results confirm their conclusions with the exception that, in this comparison, the iron contamination level is slightly higher than the chromium contamination level.

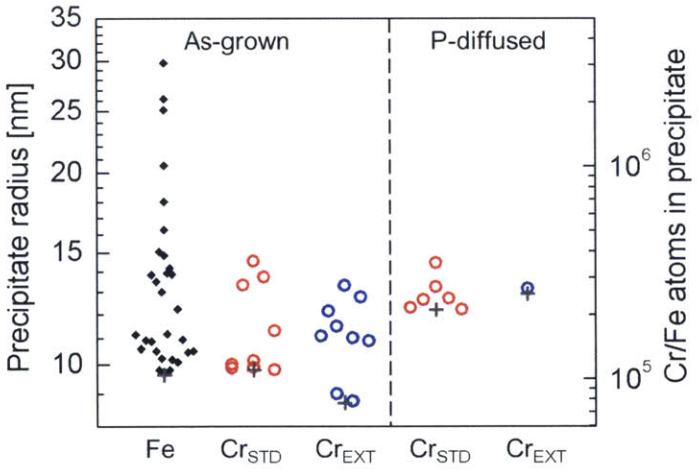

Figure 13: Comparison of chromium- and iron-rich precipitates

Precipitate distributions obtained from automated analysis of the spatially resolved maps for iron (reported in [21]) and chromium (this study). The gray "+" on each distribution represents the estimated noise floor of the measurement.

After phosphorous diffusion, some Cr-rich precipitates remain (Figure 11), while the co-located copper fluorescence is no longer detectable (Figure 12). This suggests that the phosphorus diffusion processes were insufficient to getter all precipitated metals, especially Cr, consistent with the Cr solubility estimates at the different temperatures (1.46×10^{12} cm^{-3} at 845°C and 9.01×10^{12} cm^{-3} at 920°C). After the STD process, 6 particles are identified, while after the

EXT process, 1 particle is identified. Quantitative comparisons between as-grown and phosphorus-diffused states are challenging because a small number of precipitates are identified and the μ-XRF background signal is higher for the phosphorus-diffused than for the as-grown measurements (Figure 13).

The change in background level is due to differences in measurement setup, likely the distance between the detector and the sample, confirmed by corresponding μ-XRF measurements of NIST standard reference material 1832. The MDL's associated with each μ-XRF measurement of the Cr-contaminated samples are listed in Table 1. These MDL's were calculated according to the procedure described in Section 2.3.1.

Table 1: Minimum detection limits for Cr-contaminated samples

Sample	MDL	
-	10^{-18} g	10^{4} atoms
STD - As-grown	6.53	7.56
STD - Post-gettering	7.66	8.87
EXT - As-grown	6.10	7.06
EXT - Post-gettering	7.66	8.87

For both the STD and EXT samples, the MDL is higher in the post-gettering state compared to the as-grown state. This indicates that the difference in background level as shown in Figure 13 is due to differences in measurement setup.

4.2 Detecting and gettering chromium point defects

4.2.1 Area-averaged results

Analysis of the larger samples, coupled with the μ-XRF data, provides insight into the evolution of the total chromium concentration in the wafer after gettering. Lifetimes (Cr_i, Δn = 10^{15} cm^{-3}) and interstitial concentrations as measured by QSSPC before and after gettering are shown in Figure 14. For each sample, the chromium concentration is taken to be the median value across the full range of measured injection levels, excluding trapping regimes. Calculated chromium concentrations requiring less than 1% measurement precision based on the lifetime and injection level are excluded. The as-grown interstitial concentration constitutes roughly one-

half of the total estimated chromium concentration, with the remaining chromium assumed to be in precipitated form as observed by μ-XRF. Both time-temperature profiles result in average lifetime increases from 0.1 to at least 10 μs and [Cr_i] reductions from 10^{13} to 10^{10} cm^{-3}. The decrease in [Cr_i] by phosphorous diffusion confirms previous observations [35], [37], [38].

Process	Lifetime [μs]	Chromium [cm^{-3}]
As-grown	0.18 ± 0.04	$(4.5 \pm 0.8)\times10^{13}$
STD	15.0 ± 3.2	$(2.3 \pm 0.6)\times10^{10}$
EXT	25.7 ± 14.4	$(3.1 \pm 1.2)\times10^{10}$

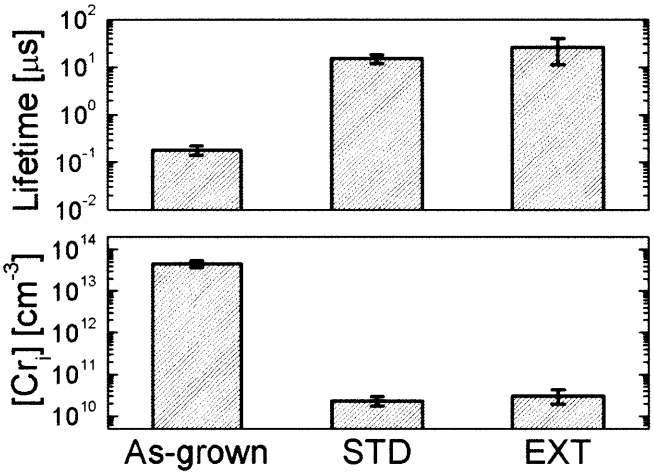

Figure 14: Average lifetime and chromium point defect concentrations

Average lifetime at $\Delta n = 10^{15}$ cm^{-3} (middle) and [Cr_i] (bottom) for three samples in each process state. Error bars represent the standard deviations of the measurements.

To assess the impact of Cr on the wafer lifetime and eventual solar cell performance, I compared the SRH lifetime, Equations (9)–(11), associated with the measured [Cr_i] to the apparent minority carrier lifetime. The recombination mechanism with the lowest lifetime will dominate the apparent lifetime, as discussed in Section 2.1.5. In the as-grown state, the Cr_i-limited SRH lifetime at 10^{15} cm^{-3} injection is 0.2 μs, indicating that the as-grown wafer lifetime is dominated by the Cr contamination. Post-gettering, the Cr_i-limited lifetimes are 413 and 309 μs for STD and EXT, respectively. The effective lifetimes measured post-gettering are significantly lower than the theoretical Cr-limited lifetimes. Some of the lifetime improvement compared to the as-grown state should be attributed to gettering of iron and/or other impurities, but the decrease in [Cr_i] is clearly an important factor.

4.2.2 Spatially resolved results

Both the STD and EXT processes are, on average, effective at externally gettering chromium to reduce the total concentration. No consistent difference in final lifetime or $[Cr_i]$ between the two processes is observed (Figure 14). However, upon closer inspection, the $[Cr_i]$ distributions after the two processes are non-uniform within the wafers. This is seen in Figure 15, part b, which features a representative pair of sister samples with both regions of comparatively lower $[Cr_i]$ after STD and lower $[Cr_i]$ after EXT. Spatially resolved maps of $[Fe_i]$ have been included to supplement the gettering discussion. In these images, concentrations lower than the pixel-by-pixel calculated detection limit are replaced with a singular low value and appear white. As-grown lifetime images (Figure 15a) display low lifetime overall with higher lifetime denuded zones at grain boundaries.

To evaluate the effect of the two processes on these different regions, I have defined three areas for comparison. In all areas, $[Fe_i]$ is lower after the EXT process, confirming the results reported in [22]. Area 1 (blue circles) contains a large grain of low dislocation density surrounded by other regions of low dislocation density. Lifetime is higher in this area after the EXT compared to the STD process in which $[Cr_i]$ is near the detection limit. Area 2 (green circles) contains medium dislocation density regions in which lifetime is higher and $[Cr_i]$ is lower after the EXT process compared to the STD process. Area 3 (red circles) contains high dislocation density regions with higher lifetime and $[Cr_i]$ after the EXT process. Our PL setup does not include corrections for lateral carrier diffusion due to inhomogeneous excess carrier densities [76], [90], photon scattering or reabsorption within the sample [91], or photon spreading within the sensor [92], [93], all of which may impact the spatial information especially in inhomogeneous areas. The setup was constant for all measurements; the trends in $[Cr_i]$ are therefore conserved but measurement artifacts are possible in Areas 2 and 3.

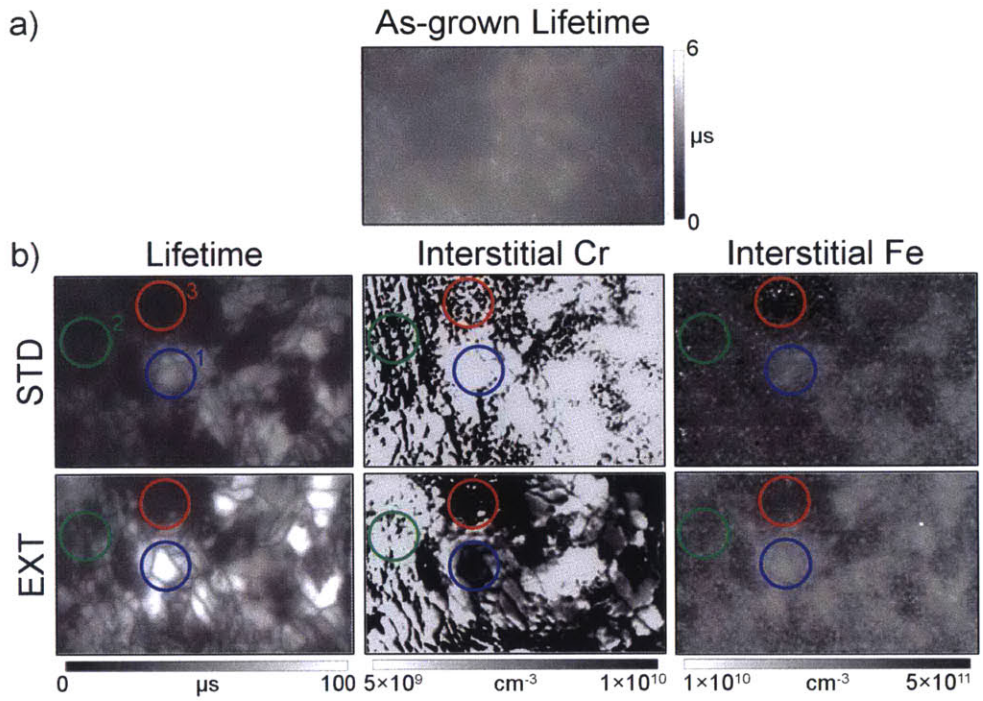

Figure 15: Spatially resolved lifetime, chromium concentration, and iron concentration

a) Spatially resolved lifetime of a representative sample in the as-grown state. b) Lifetime, [Cr_i], and [Fe_i] maps of two representative adjacent wafers, one subjected to the standard process (STD) and one subjected to the extended process (EXT). In the lifetime images, dark areas correspond to low lifetime and light areas correspond to high lifetime. In the [Cr_i] and [Fe_i] images, dark areas correspond to high concentrations and light areas correspond to low concentrations on a logarithmic scale. The solid blue, green, and red circles were selected to compare the two different gettering processes.

The results in each area can be explained by considering that the higher temperature EXT process may more effectively dissolve small Cr-rich precipitates. In areas of low dislocation density (Area 1), Cr_i atoms may be "frozen" into bulk intragranular regions during cooling. Combined with a reduction in other impurity concentrations during gettering, the remaining Cr_i ($\approx 10^{10}$ cm^{-3}) in these intragranular, high-lifetime regions can contribute significantly to the local performance (≈20% of the total recombination rate due to Cr_i after EXT). In contrast, areas of medium and high dislocation density may differ in as-grown precipitate density due to differences in the density of heterogeneous nucleation sites. In Area 2, the EXT process appears to be sufficient and preferable to the STD process to dissolve precipitates and externally getter Cr. In Area 3, the EXT process results in frozen Cr_i atoms, but due to low lifetime presumably limited by structural defects, the Cr_i contribution to the recombination rate remains less than 5%

after both processes. Therefore, although both processes are effective at externally gettering and reducing the total concentration of Cr, the spatially resolved results after the EXT process indicate that there are some areas of incomplete external gettering that require a longer duration anneal.

4.3 Time-temperature profile design

The results presented in this thesis indicate that, similar to iron, the distribution of chromium can be engineered through gettering. The total Cr concentration was reduced by both gettering processes, with precipitates retaining their sizes after processing. Before processing, approximately 4×10^{13} cm^{-3} Cr was present in precipitated form, and 4×10^{13} cm^{-3} Cr was present in interstitial form. Assuming that the precipitate size and density are unchanged by gettering, $\approx10^{13}$ cm^{-3} Cr was removed from the wafers by gettering. This Cr is likely externally gettered, diffusing to the emitter and PSG layer as has been observed by SIMS [37], [38].

The μ-XRF results suggest that the largest Cr-rich precipitates do not decrease in size after processing. When precipitates are in close proximity to Cr_i atoms (*e.g.*, near a grain boundary), chromium may be internally gettered to existing precipitates, allowing them to retain their sizes. Small Cr-rich precipitates may be dissolved by the processes applied, but it is difficult to make strong conclusions due to the μ-XRF minimum detection limit. If one half of the total Cr concentration is in precipitated form ($\approx4\times10^{13}$ cm^{-3} as stated previously), a temperature of ≈990°C would be required to fully dissolve precipitates, or to achieve a solid solubility equal to the precipitated concentration. High diffusion temperatures up to 1100°C have previously been tested and resulted in low lifetimes in mc-Si samples due to an unknown defect [94]. The high diffusion temperature suggested here is derived from the chromium contamination concentration, which is much higher than that in industrial ingots. For an industrial sample, a lower diffusion temperature would be required, thus avoiding this lifetime degradation at high temperatures.

As observed in the previous section, a higher diffusion temperature implemented without an adequate anneal or slow cool may lead to localized lifetime degradation due to interstitial atoms. This observation is consistent with diffusion gettering profile design principles outlined in [82]. The EXT process employed herein consisted of a 600°C low-temperature anneal with a cooling rate of 4–5°C/min to 600°C. While sufficient for iron, this anneal was insufficient to externally getter all of the dissolved Cr_i, likely due to the lower diffusivity of chromium compared to iron.

An annealing temperature of ≈760°C would achieve a chromium diffusivity of 1.5×10^{-7} cm^2/s, the same as iron at 600°C. Therefore, to dissolve Cr-rich precipitates and prevent localized degradation due to Cr_i, an annealing step at 760°C should be implemented with a diffusion temperature of 990°C.

CHAPTER

5

DESIGNING LIFETIME SPECTROSCOPY FOR DEFECT DETECTION IN HIGH PURITY MATERIALS

High lifetimes in industrial crystalline silicon materials, in some cases exceeding 1 ms [13], [95], can often be attributed to significant reductions in impurity concentrations. Further material improvement through identification of limiting impurities demands measurement techniques capable of detecting even lower impurity concentrations. The techniques employed in Chapters 3 and 4 in this thesis were successful in elucidating the gettering kinetics of chromium in highly contaminated crystalline silicon for research purposes; however, contamination levels on the order of 10^{13} cm^{-3} with as-grown lifetimes less than 1 μs are not likely in industrial operations that have been optimized to achieve maximum solar cell efficiency. Depending on the solar cell architecture, target efficiency, and impurity, allowable contamination concentrations can be below 10^{10} cm^{-3} [18].

Current techniques, including μ-XRF and metastable lifetime spectroscopy, are not sensitive enough to support high-efficiency crystalline silicon materials. The likelihood of detecting impurities with μ-XRF at 2-ID-D depends on the impurity type, growth conditions, and nucleation site density. For example, for iron in mc-Si, a contamination level on the order of 10^{14} cm^{-3} may be necessary to form observable precipitates in the material. If precipitates are not present, the impurity is likely not detectable at the beamline. The detection limit achieved by PLI-based metastable defect lifetime spectroscopy in this thesis was stated to be $\approx 5\times10^{9}$ cm^{-3} in the highest lifetime areas. However, these techniques are limited to iron, chromium, and oxygen in boron-doped crystalline silicon. Iron and chromium have been demonstrated to be getterable; as time-temperature profiles and manufacturing processes are refined, other impurities may begin to dominate the lifetime, and the required detection limit will likely drop below 10^{9} cm^{-3}.

Further, as the industry embraces *n*-type silicon as a bulk material for solar cells, metastable techniques that rely on association and dissociation of point defects with boron are not applicable.

One promising approach for measuring low concentrations of impurities in high-performance crystalline silicon, mentioned in Section 2.3.3, is temperature- and injection-dependent lifetime spectroscopy (TIDLS). This technique has the potential to quantify impurity concentrations for a wide range of semiconductor materials, impurity types, and contamination levels. If the impurity degrades the measured lifetime, information can be gleaned from a TIDLS measurement. The detection limit depends on the magnitude of the relative lifetime contributions, the ability to extract the SRH lifetime across a wide injection range, and the temperature range available for measurement. A mid-gap asymmetric impurity, for example, requires a wide temperature range of almost 600 K [41]. Previous implementations of TIDLS have used the technique to study defect parameters in highly contaminated materials [27], [41], [96]. Further, some of these implementations have suffered from a narrow temperature range or an average lifetime measurement over a large sample area. With recent advancements in high-performance crystalline silicon materials, TIDLS has the opportunity to play a significant role in further development through identification and mitigation of lifetime-limiting impurities. In the following sections, I present the design of a TIDLS characterization tool, initial measurements taken with the tool, and a summary of next steps required for development.

5.1 TIDLS characterization tool design

Building upon prior work in the laboratory, I propose the development of a TIDLS system based on a free carrier absorption lifetime measurement that was developed to separate surface and bulk lifetime contributions in thin silicon wafers [97]. Free carrier absorption (FCA), described briefly in Section 2.1.6, is a transient lifetime measurement that tracks optical interactions of pump and probe light beams with the material. This approach offers several advantages over previous TIDLS implementations, including enhanced spatial resolution and more flexibility in terms of thickness, passivation quality, impurity type, and impurity concentration. In contrast to the Sinton Instruments WCT-120, which averages lifetime over a circular 40 mm diameter area, the FCA system has a small and tunable spot size. A wide range of injection levels can be achieved, and the temperature stage selected offers a temperature range of

more than 600K, allowing detection of a wide range of impurities. The wavelength of the pump beam can also be varied to separate bulk and surface lifetimes.

By varying the wavelength of the pump beam, carriers can be generated in different depths into the material. As shown in Figure 16, light absorption in silicon is governed by the Beer-Lambert law (similar to Equation (3)) and varies through the material thickness. For long wavelengths below the bandgap energy, incident light is transmitted at 100% ($I_t/I_0 = 1$); for short wavelengths, incident light is absorbed near the surface. For example, a wavelength of 1050 nm results in a nearly uniform carrier generation profile in silicon at room temperature, assuming that every absorbed photon results in an electron-hole pair. Therefore, varying the pump wavelength allows the probe beam to sample carriers near the front surface or in the material bulk. Comparing measurements of lifetime near the surface and lifetime in the bulk enables estimation of surface recombination velocities in crystalline silicon at room temperature [97].

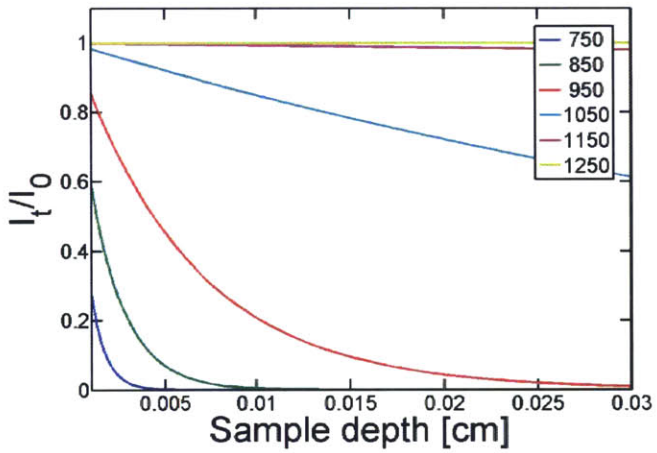

Figure 16: Wavelength dependence of photon absorption in c-Si

The transmitted fraction of photons according to the Beer-Lambert law is plotted versus silicon sample depth for wavelengths ranging from 750 nm to 1250 nm. The bandgap of silicon is 1.124 eV, or about 1100 nm. Short wavelengths are absorbed near the front surface of the material, while long wavelengths below the bandgap energy are not absorbed at all. A wavelength of approximately 1050 nm is relatively uniformly absorbed throughout the thickness. Wavelength-dependent absorption coefficient data is taken from [11].

Figure 17 depicts a characterization tool including a free-carrier absorption setup integrated with an off-the-shelf temperature stage from Linkam Scientific Instruments [98]. The LTS420 temperature stage consists of a heating block that controls the sample temperature between 77K

and 690K using an electric heater and enclosed liquid nitrogen flow, vented to atmosphere. The heating block and temperature stage are oriented vertically so that the sample lies perpendicular to the pump and probe beam planes. In the horizontal plane, parallel to the surface of the optical table, the probe beam is oriented at 90° to the sample surface, and the pump beam is offset at an angle. The temperature stage can be purged with dry nitrogen gas either before or during a measurement. This prevents condensation on the sample surface, which can inhibit the optical measurement. A circular aperture in the heating block with 4 mm diameter allows the pump beam to pass through the sample, and there are two quartz windows with 22 mm diameter on the front and back of the temperature stage.

In the current setup, a neodymium-doped yttrium aluminum garnet (Nd:YAG) laser provides a 6 ns full-width half-maximum pump pulse at a variable wavelength. Nd:YAG is a common material used for solid-state infrared lasers, and the 6 ns pulse width is sufficient to measure lifetimes in crystalline silicon, which are in most cases greater than 1 μs. The Nd:YAG laser beam passes through a series of harmonic-generating crystals that are used to modulate the output wavelength. For bulk measurements at room temperature, the pump wavelength is set to 1050 nm, while for surface measurements, a wavelength of 750 nm has been used [97]. For robust temperature-dependent measurements, the pump wavelength should either be changed as a function of temperature or set to a value of 1000 nm to account for bandgap narrowing [41]. A halogen lamp equipped with a monochromator emits a continuous wave probe beam at 1550 nm (≈ 0.80 eV), and the probe detector is InGaAs (0.75 eV direct bandgap) connected to a 40 dB amplifier and an Agilent Infiniium oscilloscope. The wavelength of the probe beam is selected so the energy is less than the bandgap of silicon and carriers are not generated by the probe. Free carriers will readily absorb these low energy photons. A probe beam (and corresponding detector) with even lower energy and higher power would result in a stronger free carrier absorption response. An additional detector monitors the pump pulse to trigger a measurement of the transient probe beam absorption. LabVIEW is used to collect time-resolved data from both detectors.

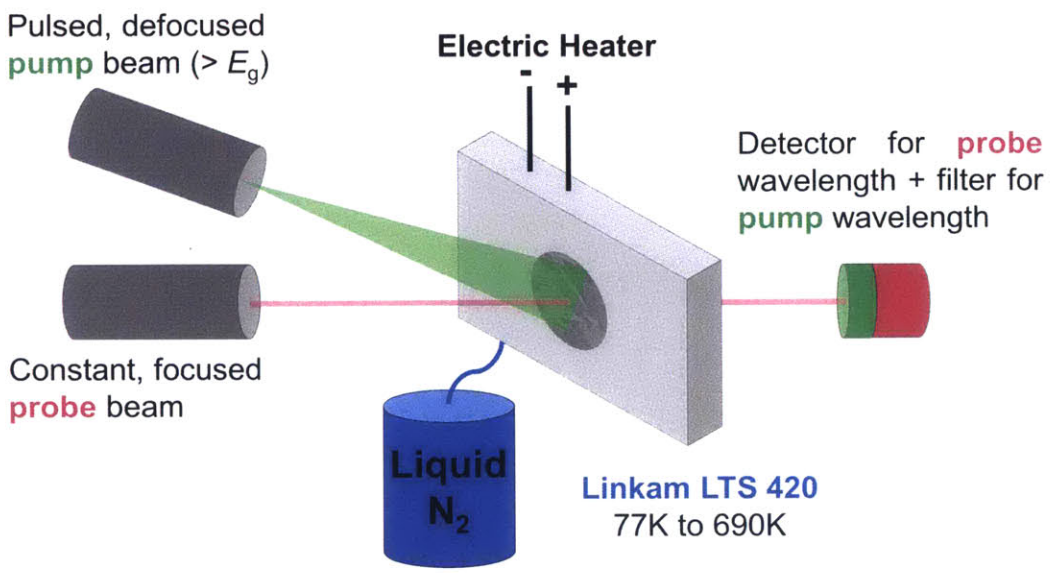

Figure 17: Proposed setup for temperature- and injection-dependent lifetime spectroscopy

A free carrier absorption pump-probe system is integrated with an off-the-shelf temperature stage to facilitate injection-dependent lifetime measurements of silicon at a range of steady-state sample temperatures.

5.2 Initial TIDLS measurements of Czochralski silicon

As a proof-of-concept experiment for this tool, initial measurements have been made on single-crystalline Czochralski silicon. The sample is 275 μm thick with a resistivity of 3.9 Ω-cm (equivalent *p*-type B-doping concentration of $\approx 3.5\times10^{15}$ cm^{-3}). This sample was gettered according to the STD process and passivated with Al_2O_3 as described in Section 3.2. At an injection level of 10^{15} cm^{-3}, the minority carrier lifetime measured by QSSPC is 750–800 μs.

For the FCA measurement, the sample was placed so that the sample center was aligned with the aperture in the heating block. The pump wavelength was 1050 nm for all temperatures. The sample was measured at 20°C, 75°C, and 125°C. The sample temperature was taken to be the heating block temperature, recorded by a thermocouple integrated with the LTS420. Prior to measurement, the temperature stage was purged with high-purity nitrogen for 5 min according to the procedure specified by Linkam [98]. The free carrier absorption response (InGaAs detector voltage) was measured after each of 5,000 pulses and then averaged to produce a single curve at each temperature. By averaging the response of the material to a large number of pulses, the measurement noise can be reduced. A measurement was taken at room temperature (25°C) just after the 125°C measurement as an accuracy check.

Figure 18 contains the measurement results. Figure 18a plots the measured detector voltage versus time. At the time of the pulse, probe beam absorption is at a maximum and the detector voltage is at a minimum. For data processing, the voltage-time data has been adjusted to remove any voltage offset with respect to the non-pumped state and has been inverted so that maximum absorption corresponds to maximum voltage. This is what is shown in Figure 18a. After the pulse, carriers recombine and probe beam absorption decreases. As temperature increases, the measured absorption at a given time is higher, indicating a higher lifetime.

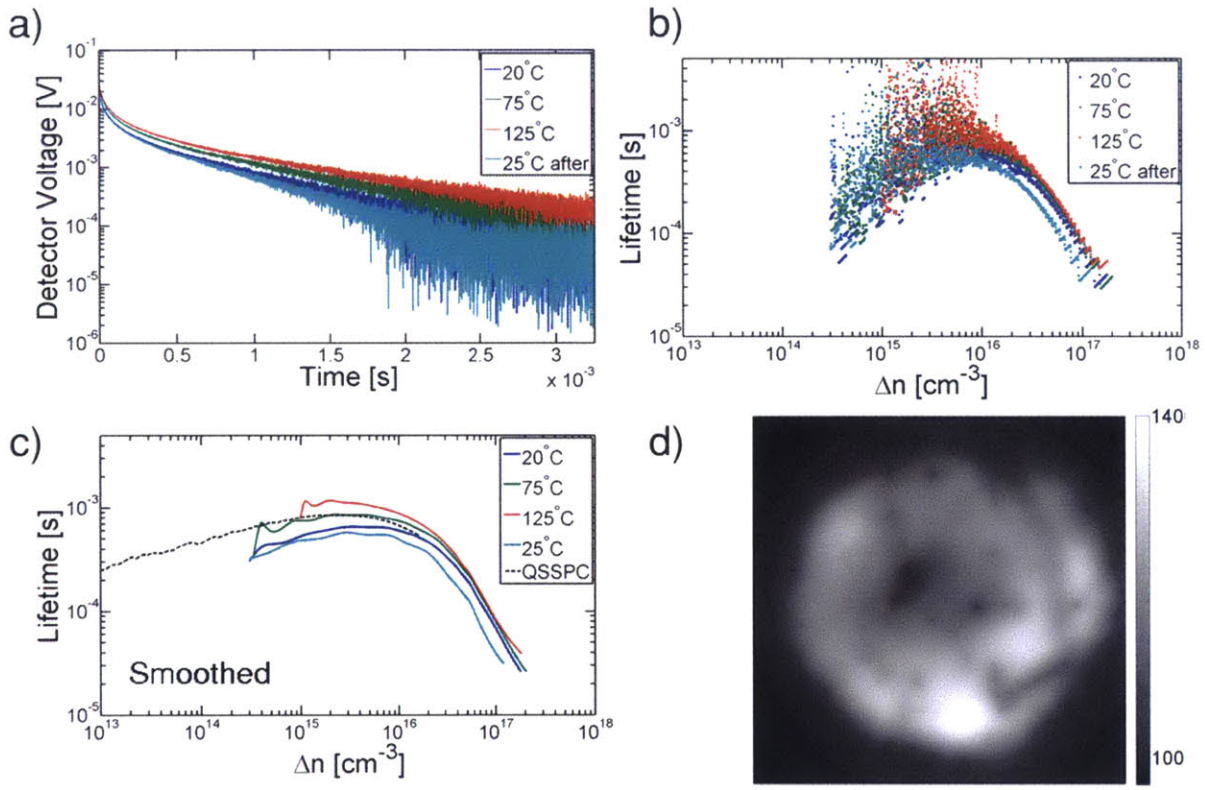

Figure 18: Free carrier absorption measured at three different temperatures

Free carrier absorption was used to measure the minority carrier lifetime of a *p*-type Czochralski sample between room temperature and 125°C. a) Detector voltage measured as a function of time at each temperature. b) Lifetime curves obtained by processing the data shown in part a according to the free carrier absorption coefficient and transient lifetime equations. c) Lifetime curves smoothed by spline-fitting the excess carrier density as a function of time prior to the lifetime calculation. The black dotted line represents the lifetime measured by QSSPC. d) PLI of the measured Cz sample, indicating areas of locally low lifetime near the center of the sample.

Absorption by free carriers is governed by the Beer-Lambert law. Assuming that detector voltage is directly proportional to transmitted light intensity, the following equations can be used to process the voltage decay into carrier concentration as a function of time:

$$I_t(W) = I_P \exp\left(-\alpha_{eq} W - \alpha_{FCA} W\right) = I_0 \exp(-\alpha_{FCA} W) \tag{28}$$

$$\alpha_{FCA} = \sigma_n \Delta n + \sigma_p \Delta p = \sigma_{FCA} \Delta n \tag{29}$$

where I_t is the intensity of transmitted light, I_0 is the intensity of incident light, α_{FCA} is the free carrier absorption coefficient, W is the sample thickness, and σ_n and σ_p are absorption cross-sections for electrons and holes (different from the capture cross-sections used to calculate SRH lifetime). The excess electron and hole populations are assumed to be equal, and σ_{FCA} is the ambipolar absorption cross-section ($\sigma_n + \sigma_p$). The free-carrier absorption coefficient is enhanced at injection levels greater than 3×10^{16} cm^{-3}; the corrections suggested by [99] have been used to calculate the data presented herein. An ambipolar coefficient equal to 1.5×10^{-17} cm^{-3}, reported in [97], is assumed with equal contributions from electrons and holes. The temperature dependence of the FCA coefficient is accounted for by assuming a linear scaling with respect to the value at room temperature, as suggested by the experiments presented in [100].

Figure 18b contains the lifetime data, processed according to the transient version of Equation (2) and plotted versus injection level. The raw data was binned before the calculation, accounting for the diagonal lines in each curve. The data is very noisy starting at 10^{16} cm^{-3} injection; data quality can be improved by including more pulses in the average. In addition, it should be noted that the measured sample is only single-side polished. Roughness on either side of the sample can result in scattered photons, reducing the intensity of the probe beam at the detector and decreasing the signal-to-noise ratio of the measurement. For easier interpretation, the data was smoothed by spline-fitting the time-dependent carrier concentration curves prior to the lifetime calculation.

The smoothed data is presented in Figure 18c, with the QSSPC results represented by the black dotted line. As suggested by the raw data, the lifetime increases with increasing temperature, with the exception of the 25°C measurement taken after the temperature ramp. This difference between the 20°C and 25°C measurements could be due to incomplete nitrogen purging and condensation on the sample; mechanical design changes are required to mitigate this issue. An alternative explanation for this lifetime discrepancy at room temperature is modification of a defect in the material, either at the surface or within the bulk. Cz silicon is

known to have high oxygen concentrations; in *p*-type materials, oxygen pairs with boron to degrade lifetime. The BO-complex is activated by illumination, and pair formation occurs more rapidly at elevated temperatures [76].

The lifetime measured by FCA at room temperature is slightly lower than that measured by QSSPC. There are several possible explanations for this. First, the diffusion length of carriers in the sample is approximately 0.16 cm. With a pump beam size of $\approx$1 cm^2, the probe beam must be centered inside the pump beam diameter to prevent edge effects (excited carriers diffusing out of the sampled area). Second, simplifying assumptions for the free-carrier absorption coefficient were made for the calculation, especially at high temperatures. The ambipolar free-carrier absorption coefficient was assumed to be composed of equal contributions from electrons and holes, and the free-carrier absorption coefficient was assumed to scale linearly with temperature. Neither of these assumptions is strictly correct according to theory [99]. Finally, the measurement may have sampled an area of locally low lifetime, indicated by the photoluminescence image in Figure 18d. Near the center of the sample, there is a dark area that corresponds to lower lifetime.

5.3 Next steps for tool development

The initial measurements presented in the previous section illustrate the potential of this characterization tool to perform TIDLS. The target materials for investigation by this tool are crystalline silicon wafers from industry, where the lifetime is limited by one or two unknown defects. The characterization tool must therefore be flexible in terms of sample thickness, doping level and type, impurity type and concentration, and passivation layer. Several design challenges remain, including purging and sealing the chamber to prevent condensation on the sample, optimizing the alignment and sizes of the two beams to allow measurement of a wide range of lifetimes, and integrating a thermocouple to measure sample surface temperature. In addition to fine-tuning the setup, the free carrier absorption coefficient should be measured as a function of temperature to ensure accuracy. A series of FCA coefficient measurements have been reported in the literature for a finite set of temperatures and specific wavelengths (such as the results reported in [100]), but neither the temperature range nor wavelengths are sufficient for the setup proposed in this thesis. The FCA coefficient can be estimated by measuring the power of the pump beam at low injection (achieved with a series of attenuation filters) and correlating this

measured power intensity to a detector voltage at the time of the pulse. In this setup, as before, each photon is assumed to generate an electron-hole pair. By performing this measurement across the temperature range and at different injection levels (though still in low injection), the FCA coefficient can be estimated with a certain precision as a function of temperature.

Especially at low injection, the signal-to-noise ratio of the measurement is crucial. The lifetimes measured in this thesis can be presented with confidence down to 5×10^{14} cm^{-3}, which is not sufficient to fit the full SRH equations for defect parameter extraction. Double-side polished, thick (>300 μm) samples can be measured in the current setup with a wider injection range. To improve the range and flexibility of the tool, a longer wavelength probe beam should be investigated. The FCA coefficient is a function of λ^2, and a longer wavelength would result in stronger absorption by free carriers [99].

After TIDLS measurements, the SRH lifetime must be extracted and fitted from the measured effective lifetime. The contributing recombination mechanisms were described in Chapter 2. As an example, the SRH lifetime was extracted from the lifetime measurements presented in the previous section. To estimate the surface lifetime, a float-zone wafer of similar resistivity was treated with the same passivation layer and the lifetime was measured by QSSPC. Assuming recombination is due only to the surface (12) and intrinsic (8) mechanisms, an injection-dependent SRV was calculated (Figure 19a). This SRV was assumed to be constant with temperature for the Cz sample. The intrinsic lifetime for the Cz sample was calculated as a function of temperature using models for temperature-dependent carrier concentration, bandgap, and radiative recombination coefficient [41]. The extracted SRH lifetimes for the Cz sample at each temperature are shown in Figure 19b. The attainable injection range is limited due to the different measurement tools (QSSPC *vs.* FCA). A key area for improvement for the TIDLS characterization tool is determining a method for measuring surface lifetime as a function of both temperature and injection.

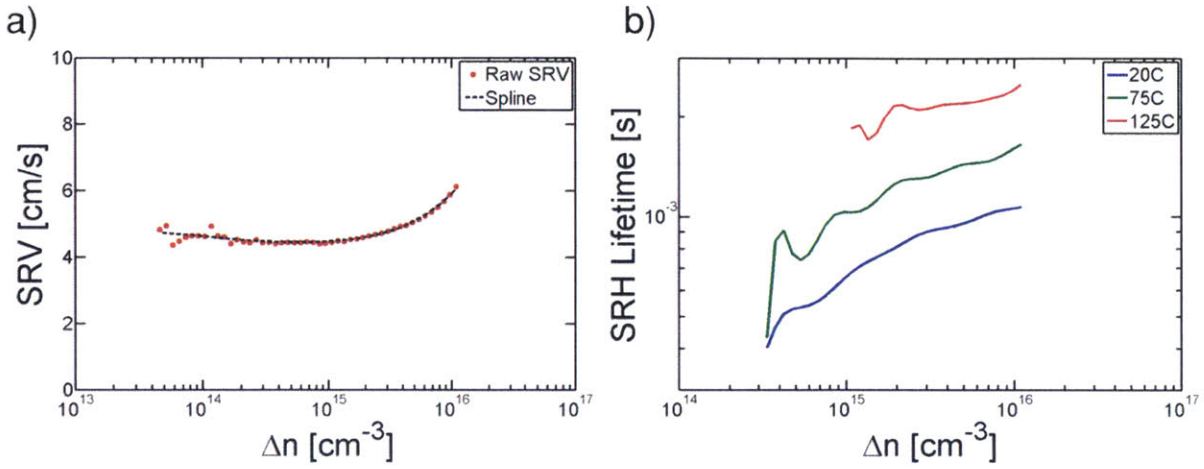

Figure 19: Extracting Shockley-Read-Hall lifetime as a function of temperature and injection level

The data shown in Figure 18 was processed to extract the SRH lifetime for the Cz sample. a) Injection-dependent surface recombination velocity at room temperature calculated by measuring the lifetime of a float-zone wafer by QSSPC and assuming the contributing recombination mechanisms are limited to surface, Auger, and radiative. b) SRH lifetime for the Cz sample at each measured temperature, assuming the SRV calculated in part a.

The SRH parameters can be extracted using the method described in Section 2.3.3 and [80]; an alternative method involves producing the defect parameter solution surface (DPSS), or plots of all possible fit parameters for each injection-dependent curve. In this method, proposed by [41], the defect is assumed to lie somewhere within the bandgap. At each valid defect level, the remaining fit parameters are the SRH parameters k and τ_{n0} or τ_{p0}. The true values of the defect level, ratio of capture cross-sections, and electron or hole capture time constant are determined by analyzing the intersections of the different DPSS curves.

CHAPTER

6

SUMMARY & CONCLUSIONS

Decreasing the cost photovoltaic modules is an important step toward encouraging widespread, global adoption of solar power. With 90% market share, silicon is a robust material for solar cells with proven bankability. Minority carrier lifetime, measured on the wafer prior to solar cell fabrication, is an indicator of solar-to-electricity conversion efficiency. Metal impurities are highly detrimental to minority carrier lifetime in silicon, especially when present in interstitial or substitutional form. Less studied than iron, chromium can degrade solar cell efficiencies in both *p*- and *n*-type silicon at concentrations as low as 10^{10} cm^{-3}. I hypothesize that the distribution of chromium in silicon can be engineered through design of time-temperature profiles for phosphorous diffusion gettering to reduce the impact on solar cell efficiency.

In this thesis, I employed impurity detection techniques, including μ-XRF, lifetime, and $[Cr_i]$ measurements, to quantify the as-grown distributions and gettering response of precipitated and interstitial chromium in mc-Si. I confirmed the smaller size of as-grown Cr-rich precipitates compared to iron-rich precipitates, consistent with diffusion-limited precipitation. In addition, Cr_i point defects account for nearly one-half of the total Cr in the as-grown material. After phosphorous diffusion gettering, minority carrier lifetime is increased by two orders of magnitude from 0.18 to 25.7 μs and $[Cr_i]$ is reduced by three orders of magnitude from 10^{13} to 10^{10} cm^{-3}. I concluded that some Cr was externally gettered, but due to the high initial concentration and the existence of Cr-rich precipitates, the gettering processes tested were not sufficient for complete removal of chromium. An even higher diffusion temperature is required to dissolve all precipitates (estimated ≈990°C in this case). To prevent localized lifetime degradation due to Cr_i after gettering, an annealing step (≈760°C) should be implemented with sufficient temperature and time to allow for complete external gettering during cooling.

This research illuminates the need for a more sensitive defect characterization technique. Chromium concentrations on the order of 10^{10} cm^{-3}, near the detection limit of the techniques

employed in this thesis, were observed to impact lifetime in intragranular regions of mc-Si after gettering. In Chapter 5, I presented a concept for a defect characterization tool that integrates free carrier absorption with a temperature stage to accomplish temperature- and injection-dependent lifetime spectroscopy. Proof-of-concept measurements on a sc-Si wafer were presented, and a path for tool improvement was outlined.

In summary, the research presented in this thesis provides quantitative information regarding the distribution of chromium in multicrystalline silicon and its gettering response, which can be used to design kinetics process simulation tools for chromium gettering in both *p*- and *n*-type silicon. In addition, I recognize the need for a more sensitive defect identification technique and outline the development of a temperature- and injection-dependent lifetime spectroscopy tool that will help to maintain the pace of innovation for high-performance silicon materials.

REFERENCES

[1] J. Jean, P. R. Brown, R. L. Jaffe, T. Buonassisi, and V. Bulovic, "Pathways for Solar Photovoltaics," *Energy Environ. Sci.*, 2015.

[2] International Energy Agency, "Technology Roadmap: Solar Photovoltaic Energy," 2010.

[3] A. Goodrich, T. James, and M. Woodhouse, "Residential, Commercial, and Utility-Scale Photovoltaic (PV) System Prices in the United States: Current Drivers and Cost-Reduction Opportunities," *NREL Tech. Rep.*, 2012.

[4] D. M. Powell, M. T. Winkler, H. J. Choi, C. B. Simmons, D. B. Needleman, and T. Buonassisi, "Crystalline silicon photovoltaics: a cost analysis framework for determining technology pathways to reach baseload electricity costs," *Energy Environ. Sci.*, vol. 5, no. 3, pp. 5874–5883, 2012.

[5] D. M. Powell, M. T. Winkler, A. Goodrich, and T. Buonassisi, "Modeling the Cost and Minimum Sustainable Price of Crystalline Silicon Photovoltaic Manufacturing in the United States," *IEEE J. Photovoltaics*, vol. 3, no. 2, pp. 662–668, 2013.

[6] "International Technology Roadmap for Photovoltaic (ITRPV): 2013 Results," 2014.

[7] National Renewable Energy Laboratory, "Best Research-Cell Efficiencies," 2015. [Online]. Available: http://www.nrel.gov/ncpv/images/efficiency_chart.jpg. [Accessed: 29-Apr-2015].

[8] A. A. Istratov, H. Hieslmair, and E. R. Weber, "Iron and its complexes in silicon," *Appl. Phys. A Mater. Sci. Process.*, vol. 69, pp. 13–44, 1999.

[9] T. Buonassisi, A. A. Istratov, M. D. Pickett, M. Heuer, J. P. Kalejs, G. Hahn, M. A. Marcus, B. Lai, Z. Cai, S. M. Heald, T. F. Ciszek, R. F. Clark, D. W. Cunningham, A. M. Gabor, R. Jonczyk, S. Narayanan, E. Sauar, and E. R. Weber, "Chemical Natures and Distributions of Metal Impurities in Multicrystalline Silicon Materials," *Prog. Photovoltaics Res. Appl.*, vol. 14, no. 6, pp. 512–531, 2006.

[10] Y. M. Yang, A. Yu, B. Hsu, W. C. Hsu, A. Yang, and C. W. Lan, "Development of high-performance multicrystalline silicon for photovoltaic industry," *Prog. Photovoltaics Res. Appl.*, vol. 23, no. 3, pp. 340–351, 2013.

[11] C. Honsberg and S. Bowden, "Photovoltaic Education Network," 2014. [Online]. Available: http://pveducation.org/. [Accessed: 28-Apr-2015].

[12] D. A. Clugston and P. A. Basore, "PC1D version 5: 32-bit solar cell modeling on personal computers," in *Proceedings of the 26th IEEE Photovoltaic Specialists Conference*, 1997, pp. 207–210.

[13] D. M. Powell, J. Hofstetter, D. P. Fenning, R. Hao, T. S. Ravi, and T. Buonassisi, "Effective lifetimes exceeding 300 μs in gettered p-type epitaxial kerfless silicon for photovoltaics," *Appl. Phys. Lett.*, vol. 103, no. 26, 2013.

[14] W. Shockley and W. T. Read, "Statistics of the Recombination of Holes and Electrons," *Phys. Rev.*, vol. 87, no. 46, pp. 835–842, 1952.

[15] R. N. Hall, "Electron-Hole Recombination in Germanium," *Phys. Rev.*, vol. 8, no. 2, p. 287, 1952.

[16] J. R. Davis, A. Rohatgi, R. H. Hopkins, P. D. Blais, P. Rai-Choudhury, J. R. Mccormick, and H. C. Mollenkopf, "Impurities in Silicon Solar Cells," *IEEE Trans. Electron Devices*, vol. ED-27, no. 4, pp. 677–687, 1980.

[17] G. Coletti, "Sensitivity of state-of-the-art and high efficiency crystalline silicon solar cells to metal impurities," *Prog. Photovoltaics Res. Appl.*, vol. 21, no. 5, pp. 1163–1170, 2013.
[18] J. Schmidt, B. Lim, D. Walter, K. Bothe, S. Gatz, T. Dullweber, and P. P. Altermatt, "Impurity-related limitations of next-generation industrial silicon solar cells," *IEEE J. Photovoltaics*, vol. 3, no. 1, pp. 114–118, 2013.
[19] A. Haarahiltunen, H. Savin, M. Yli-Koski, H. Talvitie, and J. Sinkkonen, "Modeling phosphorus diffusion gettering of iron in single crystal silicon," *J. Appl. Phys.*, vol. 105, no. 2, 2009.
[20] J. Hofstetter, D. P. Fenning, M. I. Bertoni, J. F. Lelièvre, C. del Cañizo, and T. Buonassisi, "Impurity-to-efficiency simulator: predictive simulation of silicon solar cell performance based on iron content and distribution," *Prog. Photovoltaics Res. Appl.*, vol. 19, no. 4, pp. 487–497, 2011.
[21] D. P. Fenning, J. Hofstetter, M. I. Bertoni, G. Coletti, B. Lai, C. del Cañizo, and T. Buonassisi, "Precipitated iron: A limit on gettering efficacy in multicrystalline silicon," *J. Appl. Phys.*, vol. 113, no. 4, 2013.
[22] D. P. Fenning, A. S. Zuschlag, J. Hofstetter, A. Frey, M. I. Bertoni, G. Hahn, and T. Buonassisi, "Investigation of lifetime-limiting defects after high-temperature phosphorus diffusion in high-iron-content multicrystalline silicon," *IEEE J. Photovoltaics*, vol. 4, no. 3, pp. 866–873, 2014.
[23] J. Schön, H. Habenicht, M. C. Schubert, and W. Warta, "Understanding the distribution of iron in multicrystalline silicon after emitter formation: Theoretical model and experiments," *J. Appl. Phys.*, vol. 109, no. 6, 2011.
[24] J. Hofstetter, J. F. Lelièvre, C. del Cañizo, and A. Luque, "Acceptable contamination levels in solar grade silicon: From feedstock to solar cell," *Mater. Sci. Eng. B Solid-State Mater. Adv. Technol.*, vol. 159–160, pp. 299–304, 2009.
[25] G. Coletti, P. C. P. Bronsveld, G. Hahn, W. Warta, D. Macdonald, B. Ceccaroli, K. Wambach, N. Le Quang, and J. M. Fernandez, "Impact of metal contamination in silicon solar cells," *Adv. Funct. Mater.*, vol. 21, no. 5, pp. 879–890, 2011.
[26] H. Conzelmann, K. Graff, and E. R. Weber, "Chromium and chromium-boron pairs in silicon," *Appl. Phys. A Solids Surfaces*, vol. 30, no. 3, pp. 169–175, 1983.
[27] J. Schmidt, R. Krain, K. Bothe, G. Pensl, and S. Beljakowa, "Recombination activity of interstitial chromium and chromium-boron pairs in silicon," *J. Appl. Phys.*, vol. 102, no. 12, 2007.
[28] S. Dubois, O. Palais, and P. J. Ribeyron, "Determination at 300 K of the hole capture cross section of chromium-boron pairs in p-type silicon," *Appl. Phys. Lett.*, vol. 89, no. 23, pp. 22–25, 2006.
[29] S. Dubois, O. Palais, P. J. Ribeyron, M. Pasquinelli, S. Martinuzzi, and J. Dugas, "Dissolved chromium in crystalline silicon - detection and impact on solar cell performances," in *Proceedings of the 22nd EU-PVSEC*, 2007, pp. 1193–1196.
[30] H. Habenicht, M. C. Schubert, and W. Warta, "Imaging of chromium point defects in p-type silicon," *J. Appl. Phys.*, vol. 108, no. 3, 2010.
[31] K. Mishra, "Identification of Cr in p-type silicon using the minority carrier lifetime measurement by the surface photovoltage method," *Appl. Phys. Lett.*, vol. 68, p. 3281, 1996.
[32] G. Zoth and W. Bergholz, "A fast, preparation-free method to detect iron in silicon," *J. Appl. Phys.*, vol. 67, no. 11, pp. 6764–6771, 1990.

[33] N. T. Bendik, V. S. Garnyk, and L. S. Milevskii, "Precipitation kinetics of solid solutions of chromium in silicon," *Sov. Phys. - Solid State*, vol. 12, no. 1, pp. 190–195, 1970.
[34] J. B. Mohr, S. H. Park, S. N. Schauer, D. K. Schroder, and J. Kalejs, "Physical and Electrical Investigation of Silicide Precipitates in EFG Polycrystalline Silicon Intentionally Contaminated with Chromium," in *Proceedings of the 21st IEEE Photovoltaic Specialists Conference*, 1990, pp. 711–716.
[35] J. Schön, H. Habenicht, W. Warta, and M. C. Schubert, "Chromium distribution in multicrystalline silicon: comparison of simulations and experiments," *Prog. Photovoltaics Res. Appl.*, vol. 21, no. 4, pp. 676–680, 2013.
[36] F. D. Heinz, F. Schindler, W. Warta, and M. C. Schubert, "Interstitial Chromium in Silicon on the Micron Scale," in *Energy Procedia*, 2013, vol. 38, pp. 571–575.
[37] S. E. Asher, J. P. Kalejs, and B. Bathey, "SIMS analysis of chromium gettering in crystalline silicon," *AIP Conf. Proc.*, vol. 268, pp. 409–412, 1992.
[38] A. Bentzen, A. Holt, R. Kopecek, G. Stokkan, J. S. Christensen, and B. G. Svensson, "Gettering of transition metal impurities during phosphorus emitter diffusion in multicrystalline silicon solar cell processing," *J. Appl. Phys.*, vol. 99, no. 9, pp. 1–6, 2006.
[39] D. Bouhafs, N. Khelifati, and A. Boucheham, "Optimized temperature in Phosphorous Diffusion Gettering (PDG) setup of chromium transition metal in solar grade multicrystalline silicon P-type wafers," in *5th International Advances in Applied Phyiscs and Materials Science Congress & Exhibition*, 2015.
[40] D. Macdonald, A. Cuevas, A. Kinomura, and Y. Nakano, "Phosphorus gettering in multicrystalline silicon studied by neutron activation analysis," in *Proceedings of the 29th IEEE Photovoltaic Specialists Conference*, 2002, pp. 285–288.
[41] S. Rein, *Lifetime Spectroscopy: A Method of Defect Characterization in Silicon for Photovoltaic Applications*. Springer, 2005.
[42] M. A. Green, *Silicon Solar Cells: Advanced Principles & Practice*. Syndey, N. S. W.: Centre for Photovoltaic Devices and Systems, University of New South Wales, 1995.
[43] S. Rein, T. Rehrl, W. Warta, and S. W. Glunz, "Lifetime spectroscopy for defect characterization: Systematic analysis of the possibilities and restrictions," *J. Appl. Phys.*, vol. 91, no. 3, pp. 2059–2070, 2002.
[44] J. Hofstetter, C. del Cañizo, H. Wagner, S. Castellanos, and T. Buonassisi, "Materials requirements for the adoption of unconventional crystal-growth techniques for high-efficiency solar cells," In preparation.
[45] M. A. Green, *Solar Cells: Operating Principles, Technology, and System Applications*. Kensington, New South Wales: The University of New South Wales, 1998.
[46] T. Trupke, M. A. Green, P. Würfel, P. P. Altermatt, A. Wang, J. Zhao, and R. Corkish, "Temperature dependence of the radiative recombination coefficient of intrinsic crystalline silicon," *J. Appl. Phys.*, vol. 94, no. 8, pp. 4930–4937, 2003.
[47] H. T. Nguyen, S. C. Baker-Finch, and D. Macdonald, "Temperature dependence of the radiative recombination coefficient in crystalline silicon from spectral photoluminescence," *Appl. Phys. Lett.*, vol. 104, no. 11, pp. 88–91, 2014.
[48] A. R. Beattie and P. T. Landsberg, "Auger effect in semiconductors," *Proc. R. Soc. London A*, vol. 249, pp. 16–29, 1959.
[49] A. Haug, "Carrier density dependence of Auger recombination," *Solid. State. Electron.*, vol. 21, no. 11–12, pp. 1281–1284, 1978.

[50] L. Huldt, "Band-to-band auger recombination in indirect gap semiconductors," *Phys. Status Solidi*, vol. 8, no. 1, pp. 173–187, 1971.
[51] A. Hangleiter and R. Häcker, "Enhancement of Band-to-Band Auger Recombination by Electron-Hole Correlations," *Phys. Rev. Lett.*, vol. 65, no. 2, pp. 215–218, 1990.
[52] P. P. Altermatt, J. Schmidt, G. Heiser, and A. G. Aberle, "Assessment and parameterisation of Coulomb-enhanced Auger recombination coefficients in lowly injected crystalline silicon," *J. Appl. Phys.*, vol. 82, no. 10, p. 4938, 1997.
[53] D. B. Laks, G. F. Neumark, and S. T. Pantelides, "Accurate interband-Auger-recombination rates in silicon," *Phys. Rev. B*, vol. 42, no. 8, pp. 5176–5185, 1990.
[54] P. T. Landsberg, "Trap-Auger recombination in silicon of low carrier densities," *Appl. Phys. Lett.*, vol. 50, no. 12, pp. 745–747, 1987.
[55] A. Richter, S. W. Glunz, F. Werner, J. Schmidt, and A. Cuevas, "Improved quantitative description of Auger recombination in crystalline silicon," *Phys. Rev. B - Condens. Matter Mater. Phys.*, vol. 86, no. 16, pp. 1–14, 2012.
[56] P. P. Altermatt, F. Geelhaar, T. Trupke, X. Dai, A. Neisser, and E. Daub, "Injection dependence of spontaneous radiative recombination in c-Si: Experiment, theoretical analysis, and simulation," *Proc. 5th Int. Conf. Numer. Simul. Optoelectron. Devices*, pp. 47–48, 2005.
[57] A. B. Sproul, "Dimensionless solution of the equation describing the effect of surface recombination on carrier decay in semiconductors," *J. Appl. Phys.*, vol. 76, no. 5, pp. 2851–2854, 1994.
[58] M. Cho, H. B. Park, J. Park, C. S. Hwang, J.-C. Lee, S.-J. Oh, J. Jeong, K. S. Hyun, H.-S. Kang, Y.-W. Kim, and J.-H. Lee, "Thermal annealing effects on the structural and electrical properties of HfO 2/Al 2 O 3 gate dielectric stacks grown by atomic layer deposition on Si substrates," *J. Appl. Phys.*, vol. 94, no. 4, pp. 2563–2571, 2003.
[59] G. Agostinelli, a. Delabie, P. Vitanov, Z. Alexieva, H. F. W. Dekkers, S. De Wolf, and G. Beaucarne, "Very low surface recombination velocities on p-type silicon wafers passivated with a dielectric with fixed negative charge," *Sol. Energy Mater. Sol. Cells*, vol. 90, no. 18–19, pp. 3438–3443, 2006.
[60] F.-J. Ma, G. G. Samudra, M. Peters, A. G. Aberle, F. Werner, J. Schmidt, and B. Hoex, "Advanced modeling of the effective minority carrier lifetime of passivated crystalline silicon wafers," *J. Appl. Phys.*, vol. 112, no. 5, p. 054508, 2012.
[61] R. A. Sinton and D. Macdonald, *WCT-120 Photoconductance Lifetime Test and option Suns-Voc Stage: User Manual*. Boulder, CO: Sinton Consulting, Inc., 2006.
[62] *WT-2000 User Manual*. Budapest, Hungary: Semilab Semiconductor Physics Laboratory, Inc., 2011.
[63] J. Linnros, "Carrier lifetime measurements using free carrier absorption transients. I. Principle and injection dependence," *J. Appl. Phys.*, vol. 84, no. 1, p. 275, 1998.
[64] S. Herlufsen, J. Schmidt, D. Hinken, K. Bothe, and R. Brendel, "Photoconductance-calibrated photoluminescence lifetime imaging of crystalline silicon," *Phys. Status Solidi - Rapid Res. Lett.*, vol. 2, no. 6, pp. 245–247, 2008.
[65] T. Trupke, R. Bardos, M. Schubert, and W. Warta, "Photoluminescence imaging of silicon wafers," *Appl. Phys. Lett.*, vol. 89, no. 4, p. 044107, 2006.
[66] K. Graff, *Metal Impurities in Silicon-Device Fabrication*, 2nd ed. New York, New York: Springer-Verlag, 2000.

[67] T. Buonassisi, A. A. Istratov, M. Heuer, M. A. Marcus, R. Jonczyk, J. Isenberg, B. Lai, Z. Cai, S. Heald, W. Warta, R. Schindler, G. Willeke, and E. R. Weber, "Synchrotron-based investigations of the nature and impact of iron contamination in multicrystalline silicon solar cells," *J. Appl. Phys.*, vol. 97, no. 7, pp. 1–11, 2005.

[68] T. Buonassisi, A. A. Istratov, M. D. Pickett, M. A. Marcus, T. F. Ciszek, and E. R. Weber, "Metal precipitation at grain boundaries in silicon: Dependence on grain boundary character and dislocation decoration," *Appl. Phys. Lett.*, vol. 89, no. 4, pp. 1–4, 2006.

[69] A. Haarahiltunen, H. Savin, M. Yli-Koski, H. Talvitie, M. I. Asghar, and J. Sinkkonen, "As-grown iron precipitates and gettering in multicrystalline silicon," *Mater. Sci. Eng. B Solid-State Mater. Adv. Technol.*, vol. 159–160, pp. 248–252, 2009.

[70] M. Kittler, J. Lärz, W. Seifert, M. Seibt, and W. Schröter, "Recombination properties of structurally well defined NiSi2 precipitates in silicon," *Appl. Phys. Lett.*, vol. 58, no. 9, p. 911, 1991.

[71] C. del Cañizo and A. Luque, "A Comprehensive Model for the Gettering of Lifetime-Killing Impurities in Silicon," *J. Electrochem. Soc.*, vol. 147, no. 7, p. 2685, 2000.

[72] P. S. Plekhanov and T. Y. Tan, "Schottky effect model of electrical activity of metallic precipitates in silicon," *Appl. Phys. Lett.*, vol. 76, no. 25, pp. 3777–3779, 2000.

[73] P. Villars and L. D. Calvert, *Pearson's handbook of crystallographic data for intermetallic phases*. Metals Park, OH: American Society of Metals, 1985.

[74] F. Chu, M. Lei, S. A. Maloy, J. J. Petrovic, and T. E. Mitchell, "Elastic properties of C40 transition metal disilicides," *Acta Mater.*, vol. 44, no. 8, pp. 3035–3048, 1996.

[75] D. Macdonald, J. Tan, and T. Trupke, "Imaging interstitial iron concentrations in boron-doped crystalline silicon using photoluminescence," *J. Appl. Phys.*, vol. 103, no. 7, pp. 1–8, 2008.

[76] M. C. Schubert, H. Habenicht, and W. Warta, "Imaging of Metastable Defects in Silicon," *IEEE J. Photovoltaics*, vol. 1, no. 2, pp. 168–173, 2011.

[77] D. Macdonald, T. Roth, P. N. K. Deenapanray, T. Trupke, and R. A. Bardos, "Doping dependence of the carrier lifetime crossover point upon dissociation of iron-boron pairs in crystalline silicon," *Appl. Phys. Lett.*, vol. 89, no. 14, p. 142107, 2006.

[78] Y. Dusausoy, J. Protas, R. Wandji, and B. Roques, "Structure cristalline du disiliciure de fer, FeSi2β," *Acta Crystallogr. Sect. B Struct. Crystallogr. Cryst. Chem.*, vol. 27, no. 6, pp. 1209–1218, 1971.

[79] D. H. Macdonald, L. J. Geerligs, and A. Azzizi, "Iron detection in crystalline silicon by carrier lifetime measurements for arbitrary injection and doping," *J. Appl. Phys.*, vol. 95, no. 3, pp. 1021–1028, 2004.

[80] J. D. Murphy, K. Bothe, R. Krain, V. V Voronkov, R. J. Falster, J. D. Murphy, K. Bothe, R. Krain, V. V Voronkov, and R. J. Falster, "Parameterisation of injection-dependent lifetime measurements in semiconductors in terms of Shockley-Read-Hall statistics : An application to oxide precipitates in silicon," vol. 111, no. 113709, 2012.

[81] V. Vähänissi, M. Yli-Koski, A. Haarahiltunen, H. Talvitie, Y. Bao, and H. Savin, "Significant minority carrier lifetime improvement in red edge zone in n-type multicrystalline silicon," *Sol. Energy Mater. Sol. Cells*, vol. 114, pp. 54–58, 2013.

[82] D. P. Fenning, J. Hofstetter, A. E. Morishige, D. M. Powell, A. Zuschlag, G. Hahn, and T. Buonassisi, "Darwin at High Temperature: Advancing Solar Cell Material Design Using Defect Kinetics Simulations and Evolutionary Optimization," *Adv. Energy Mater.*, vol. 4, p. 1400459, 2014.

[83] S. T. Dunham, "A Quantitative Model for the Coupled Diffusion of Phosphorus and Point Defects in Silicon," *J. Electrochem. Soc.*, vol. 139, no. 9, pp. 2628–2636, 1992.
[84] B. Michl, J. Schön, W. Warta, and M. C. Schubert, "The impact of different diffusion temperature profiles on iron concentrations and carrier lifetimes in multicrystalline silicon wafers," *IEEE J. Photovoltaics*, vol. 3, no. 2, pp. 635–640, 2013.
[85] M. Ann Jensen, J. Hofstetter, A. E. Morishige, G. Coletti, B. Lai, D. P. Fenning, and T. Buonassisi, "Synchrotron-based analysis of chromium distributions in multicrystalline silicon for solar cells," *Appl. Phys. Lett.*, In Press.
[86] E. Scheil, "Bemerkungen zur schichtkristallbildung," *Zeitschrift für Met.*, vol. 34, no. 3, pp. 70–72, 1942.
[87] D. Macdonald, A. Cuevas, A. Kinomura, Y. Nakano, and L. J. Geerligs, "Transition-metal profiles in a multicrystalline silicon ingot," *J. Appl. Phys.*, vol. 97, no. 3, 2005.
[88] Z. Cai, B. Lai, W. Yun, I. McNulty, A. Khounsary, J. Maser, P. Ilinkski, D. Legnini, E. Trakhtenberg, S. Xu, B. Tieman, G. Wimerslage, and E. Gluskin, "Performance of a High-Resolution X-Ray Microprobe at the Advanced Photon Source," in *AIP CP 521, Synchrotron Radiation Instrumentation: Eleventh US National Conference*, 1999, pp. 31–34.
[89] J. Schön, A. Haarahiltunen, H. Savin, D. P. Fenning, T. Buonassisi, W. Warta, and M. C. Schubert, "Analyses of the evolution of iron-silicide precipitates in multicrystalline silicon during solar cell processing," *IEEE J. Photovoltaics*, vol. 3, no. 1, pp. 131–137, 2013.
[90] S. P. Phang, H. C. Sio, and D. Macdonald, "Carrier de-smearing of photoluminescence images on silicon wafers using the continuity equation," *Appl. Phys. Lett.*, vol. 103, no. 19, 2013.
[91] P. Würfel, T. Trupke, T. Puzzer, E. Schäffer, W. Warta, and S. W. Glunz, "Diffusion lengths of silicon solar cells from luminescence images," *J. Appl. Phys.*, vol. 101, no. 12, p. 123110, 2007.
[92] B. Mitchell, J. W. Weber, D. Walter, D. Macdonald, and T. Trupke, "On the method of photoluminescence spectral intensity ratio imaging of silicon bricks: Advances and limitations," *J. Appl. Phys.*, vol. 112, no. 6, 2012.
[93] D. Walter, A. Fell, E. Franklin, D. Macdonald, B. Mitchell, and T. Trupke, "The impact of silicon CCD photon spread on quantitative analyses of luminescence images," *IEEE J. Photovoltaics*, vol. 4, no. 1, pp. 368–373, 2014.
[94] S. M. Scott, J. Hofstetter, A. E. Morishige, and T. Buonassisi, "Sacrificial High-Temperature Phosphorus Diffusion Gettering Process for Lifetime Improvement of Multicrystalline Silicon Wafers," in *Photovoltaic Specialist Conference (PVSC), 2014 IEEE 40th*, 2014, pp. 3014–3016.
[95] M. Kivambe, D. M. Powell, S. Castellanos, M. Ann Jensen, A. E. Morishige, K. Nakajima, K. Morishita, R. Murai, and T. Buonassisi, "Minority-carrier lifetime and defect content of n-type silicon grown by the noncontact crucible method," *J. Cryst. Growth*, vol. 407, pp. 31–36, 2014.
[96] B. B. Paudyal, K. R. McIntosh, D. H. Macdonald, B. S. Richards, and R. A. Sinton, "The Implementation of Temperature Control to an Inductive-Coil Photoconductance Instrument for the Range of 0-230C," *Prog. Photovoltaics Res. Appl.*, vol. 16, pp. 609–613, 2008.
[97] S. C. Siah, M. T. Winkler, D. M. Powell, S. W. Johnston, a. Kanevce, D. H. Levi, and T. Buonassisi, "Proof-of-concept framework to separate recombination processes in thin

silicon wafers using transient free-carrier absorption spectroscopy," *J. Appl. Phys.*, vol. 117, no. 10, p. 105701, 2015.
[98] *LTS420 Temperature Controlled Stage: User Guide*. Linkam Scientific Instruments, 2009.
[99] J. Isenberg and W. Warta, "Free carrier absorption in heavily doped silicon layers," *Appl. Phys. Lett.*, vol. 84, no. 13, pp. 2265–2267, 2004.
[100] K. G. Svantesson and N. G. Nilsson, "Determination of the temperature dependence of the free carrier and interband absorption in silicon at 1.06 μm," *J. Phys. C Solid State Phys.*, vol. 12, pp. 3837–3842, 1979.